Spectroscopic and Photophysical Properties of Hexanuclear Rhenium(III) Chalcogenide Clusters

Thomas G. Gray,‡ Christina M. Rudzinski,† Emily E. Meyer,† R. H. Holm,‡ and Daniel G. Nocera*,†

Contribution from the Department of Chemistry, Massachusetts Institute of Technology 6-335, Cambridge, Massachusetts 02139, and Department of Chemistry and Chemical Biology, Harvard University, Cambridge, Massachusetts 02138

Received September 20, 2002; E-mail: nocera@mit.edu

Abstract: The electronic, vibrational, and excited-state properties of hexanuclear rhenium(III) chalcogenide clusters based on the $[Re_6(\mu_3\text{-}Q)_8]^{2+}$ (Q = S, Se) core have been investigated by spectroscopic and theoretical methods. Ultraviolet or visible excitation of $[Re_6Q_8]^{2+}$ clusters produces luminescence with ranges in maxima of 12 500–15 100 cm^{-1}, emission quantum yields of 1–24%, and emission lifetimes of 2.6–22.4 μs. Nonradiative decay rate constants and the luminescence maxima follow the trend predicted by the energy gap law (EGL). Examination of 24 clusters in solution and 14 in the solid phase establish that exocluster ligands engender the observed EGL behavior; clusters with oxygen- or nitrogen-based apical ligands achieve maximal quantum yields and the longest lifetimes. The excited-state decay mechanism was investigated by applying nonradiative decay models to temperature-dependent emission experiments. Solid-state Raman spectra were recorded to identify vibrational contributions to excited-state deactivation; spectral assignments were enabled by normal coordinate analysis afforded from Hartree–Fock and DFT calculations. Excited-state decay is interpreted with a model where normal modes largely centered on the $[Re_6Q_8]^{2+}$ core induce nonradiative relaxation. Hartree–Fock and DFT calculations of the electronic structure of the hexarhenium family of compounds support such a model. These experimental and theoretical studies of $[Re_6Q_8]^{2+}$ luminescence provide a framework for elaborating a variety of luminescence-based applications of the largest series of isoelectronic clusters yet discovered.

Introduction

Molecular cluster chemistry, while a mature science,[1] has produced few emissive, polynuclear metal–metal bonded clusters. The low-energy d–d states of transition metal centers chronically frustrate emission by providing an efficient conduit for energy flow to the ground state.[2] For this reason, polynuclear aggregates comprising d^{10} centers of copper(I), silver(I), and gold(I) display the richest photophysics of molecular metal clusters.[3,4] For clusters involving open-shell metal d centers, the most extensive photophysics issues from among the longest-known metal clusters, the molybdenum(II) and tungsten(II) halide anions $[M_6(\mu_3\text{-}X)_8X'_6]^{2-}$ (X, X' = Cl, Br, I).[5] Structurally, the cluster comprises eight metal atoms arranged in an octahedral metal core, ligated by eight face-bridging halides and six axial donor ligands. The molybdenum chloride member, $[Mo_6Cl_{14}]^{2-}$, phosphoresces in acetonitrile with a 180-μs lifetime and an emission quantum yield of 0.19 at room temperature;[6] this

cluster is one of the longest-lived and brightest lumophores in inorganic chemistry. Such properties of the emitting triplet of $[M_6(X)_8X'_6]^{2-}$ invite opportunities for the design of electricity-to-light energy conversion schemes,[7–9] organic photooxidation cycles,[10–12] and optically based sensor applications.[13,14]

Rhenium forms a sizable family of hexanuclear chalcogenide clusters $[Re_6Q_8L_6]^z$ (Q = S, Se; L = σ-donor ligand),[15,16] which are isostructural and isoelectronic with the molybdenum- and tungsten(II)-halide clusters (Scheme 1).[17] Known in extended solid phases since 1978,[18,19] these clusters are now obtainable in molecular form through the protocol of dimensional reduction.[20,21] All rhenium(III) chalcogenide clusters are prepared by
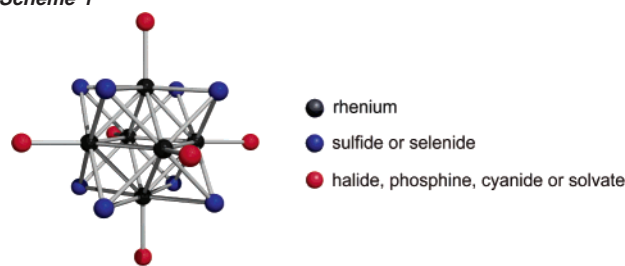
† Massachusetts Institute of Technology.
‡ Harvard University.
(1) *Metal Clusters in Chemistry*; Braunstein, P., Oro, L. A., Raithby, P. R., Eds.; Wiley-VCH: New York, 1999; Vols. 1–3.
(2) Brunold, T. C.; Güdel, H. U. In *Inorganic Electronic Structure and Spectroscopy, Volume I: Methodology*; Solomon, E. I., Lever, A. B. P., Eds.; Wiley: New York, 1999; Chapter 5.
(3) Ford, P. C.; Cariati, E.; Bourassa, J. *Chem. Rev.* **1999**, *99*, 3625.
(4) Yam, V. W. W.; Lo, K. K. K. *Chem. Soc. Rev.* **1999**, *28*, 323.
(5) Prokopuk, N.; Shriver, D. F. *Adv. Inorg. Chem.* **1998**, *46*, 1.
(6) Maverick, A. W.; Gray, H. B. *J. Am. Chem. Soc.* **1981**, *103*, 1298.

(7) Mussell, R. D.; Nocera, D. G. *J. Am. Chem. Soc.* **1988**, *110*, 2764.
(8) Mussell, R. D.; Nocera, D. G. *Inorg. Chem.* **1990**, *29*, 3711.
(9) Mussell, R. D.; Nocera, D. G. *J. Phys. Chem.* **1991**, *95*, 6919.
(10) Jackson, J. A.; Turro, C.; Newsham, M. D.; Nocera, D. G. *J. Phys. Chem.* **1990**, *94*, 4500.
(11) Jackson, J. A.; Newsham, M. D.; Worsham, C.; Nocera, D. G. *Chem. Mater.* **1996**, *8*, 558.
(12) Jackson, J. A.; Mussell, R. D.; Nocera, D. G. *Inorg. Chem.* **1993**, *32*, 4643.
(13) Ghosh, R. N.; Baker, G. L.; Ruud, C.; Nocera, D. G. *Appl. Phys. Lett.* **1999**, *75*, 2885.
(14) Ghosh, R. N.; Baker, G. L.; Ruud, C.; Nocera, D. G. *Proc. SPIE-Int. Soc. Opt. Eng.* **1999**, *3860*, 164.
(15) Bronger, W. In *Metal Clusters in Chemistry*; Braunstein, P., Oro, L. A., Raithby, P. R., Eds.; Wiley-VCH: New York, 1999; Vol. 3, p 1591.
(16) Saito, T. *J. Chem. Soc., Dalton Trans.* **1999**, 97.
(17) Perrin, A.; Perrin, C.; Sergent, M. *J. Less-Common Met.* **1988**, *137*, 241.
(18) Spangenberg, W.; Bronger, W. *Angew. Chem., Int. Ed. Engl.* **1978**, *17*, 368.
(19) Chen, S.; Robinson, W. R. *J. Chem. Soc., Chem. Commun.* **1978**, 879.

Figure 1. Electronic absorption and emission (λ_{exc} = 435.8 nm) spectra of [Re$_6$S$_8$X$_6$]$^{4-}$ clusters **1** (X = Cl, ——), **2** (X = Br, - - -), and **3** (X = I, – – –) at μM concentrations in dichloromethane. The absorption spectra are reproduced for contrast with the emission profiles; spectral intensities are normalized. Molar extinction coefficients have been previously reported (ref 20).

Figure 2. Electronic absorption spectra of [Re$_6$Q$_8$(PEt$_3$)$_6$]$^{2+}$ clusters **4** (Q = S, ——) and **5** (Q = Se, - - -) in dichloromethane. Spectral intensities are normalized.

high-temperature spontaneous self-assembly routes, often in melts. The dimensional reduction technique[22] adds equivalents of halide salts to the melt, supplying terminal ligands to the six cluster rhenium ions. Provision of 6 equiv of X$^-$ (X = Cl, Br, I) affords the discrete [Re$_6$Q$_8$X$_6$]$^{4-}$ (Q = S, X = Cl, Br, I; Q = Se, X = Cl, I); fewer equivalents generate extended solids where clusters bind one another through Re$_2$Q$_2$ rhombic interactions. Ion exchange of the as-prepared alkali metal salts of [Re$_6$Q$_8$X$_6$]$^{4-}$ with Bu$_4$N$^+$ yields clusters soluble in polar organic solvents suitable for reaction and condensed-phase spectroscopic investigations. Site-differentiation with nonlabile triethylphosphine affords species such as *cis*- and *trans*-[Re$_6$Se$_8$(PEt$_3$)$_4$(solv)$_2$]$^{2+}$ and [Re$_6$Se$_8$(PEt$_3$)$_5$(solv)]$^{2+}$ (solv = CH$_3$CN, pyridine, DMF, Me$_2$SO).[23] Fully solvated clusters are also accessible, serving as synthons for cluster-based superstructures.[24]

These synthetically versatile rhenium chalcogenides broaden the limited roster of emissive metalloclusters. They emit brilliant red phosphorescence upon UV−visible excitation, with microsecond length excited-state lifetimes.[25,26] The promise of these clusters as lumophores for a variety of light-based applications[27−32] provides an incentive to establish the fundamental factors controlling their excited-state properties. [Re$_6$Q$_8$]$^{2+}$ luminescence energies and nonradiative decay parameters have proven to be linearly related through the approximate energy gap law.[25] The emissive properties of these clusters can be optimized at the level of *synthesis*, enabling the most extensive study yet undertaken of the electronic structure and luminescence properties of polynuclear molecular clusters. We report here detailed temperature-dependent photophysical and vibrational studies of a broad family of [Re$_6$Q$_8$]$^{2+}$ cluster compounds. Quantum chemistry calculations assist in the assignments of cluster vibrational spectra and provide insight into the orbital constitution of the emitting state and the mechanism for its decay to the ground state. Taken together, these experimental and theoretical studies of [Re$_6$Q$_8$]$^{2+}$ luminescence provide a reliable
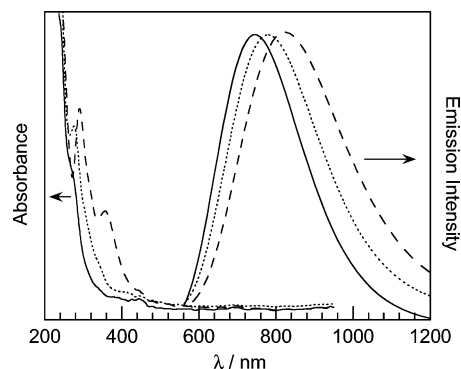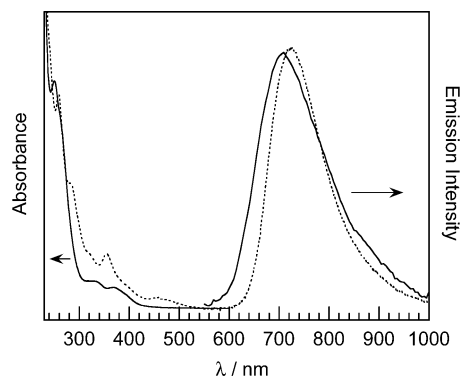
foundation for elaborating novel luminescence-based applications of the largest series of isoelectronic clusters known.

Results

Electronic Spectroscopy of [Re$_6$Q$_8$]$^{2+}$ Clusters. The electronic absorption spectra shown in Figure 1 for **1**−**3** are representative of all [Re$_6$Q$_8$L$_6$]^z cluster compounds. Closely spaced absorptions combine to form a broad, ill-resolved band in the 210−500 nm region of the spectrum.[33] Ligand-to-metal charge-transfer character of the absorption feature is confirmed by a decrease of energy of the first absorption maximum (E_{abs}) of **1**−**3** along the axial ligand series Cl > Br > I. The absorption spectra of **4** and **5** shown in Figure 2 indicate that charge-transfer contributions also originate in face-bridging chalcogenides by virtue of the red-shifted absorption profile of the selenide cluster **5** (E_{abs}(S) > E_{abs}(Se)). This spectral red shift of selenide versus sulfide clusters is maintained for all homoleptic axially ligated cluster compounds in the series.

Excitation anywhere into the absorption profile produces a broad, structureless emission extending from ∼600 to 1200 nm. The general form of the emission spectrum, shown in Figure 1 for **1**−**3**, recurs throughout the cluster series. The emission maximum (E_{em}), like E_{abs}, is mildly sensitive to variations in axial ligands about the cluster core. Table 1 summarizes E_{em}

(20) Long, J. R.; McCarty, L. S.; Holm, R. H. *J. Am. Chem. Soc.* **1996**, *118*, 4603.
(21) Long, J. R.; Williamson, A. S.; Holm, R. H. *Angew. Chem., Int. Ed. Engl.* **1995**, *34*, 226.
(22) Tulsky, E. G.; Long, J. R. *Chem. Mater.* **2001**, *13*, 1149.
(23) Zheng, Z.; Gray, T. G.; Holm, R. H. *Inorg. Chem.* **1999**, *38*, 4888.
(24) Wang, R.; Zheng, Z. *J. Am. Chem. Soc.* **1999**, *121*, 3549.
(25) Gray, T. G.; Rudzinski, C. M.; Nocera, D. G.; Holm, R. H. *Inorg. Chem.* **1999**, *38*, 5932.
(26) Yoshimura, T.; Ishizaka, S.; Umakoshi, K.; Sasaki, Y.; Kim, H.-B.; Kitamura, N. *Chem. Lett.* **1999**, 697.
(27) Gabriel, J.-C. P.; Boubekeur, K.; Uriel, S.; Batail, P. *Chem. Rev.* **2001**, *101*, 2037.
(28) Roland, B. K.; Carter, C.; Zheng, Z. *J. Am. Chem. Soc.* **2002**, *124*, 6234.
(29) Roland, B. K.; Selby, H. D.; Carducci, M. D.; Zheng, Z. *J. Am. Chem. Soc.* **2002**, *124*, 3222.
(30) Itasaka, A.; Abe, M.; Yoshimura, T.; Tsuge, K.; Suzuki, M.; Imamura, T.; Sasaki, Y. *Angew. Chem., Int. Ed.* **2002**, *41*, 463.
(31) Beauvais, L. G.; Shores, M. P.; Long, J. R. *J. Am. Chem. Soc.* **2000**, *122*, 2763.
(32) Yoshimura, T.; Umakoshi, K.; Sasaki, Y.; Ishizaka, S.; Kim, H.-B.; Kitamura, N. *Inorg. Chem.* **2000**, *39*, 1765.

(33) For a discussion of charge-transfer transitions within cyanide-bridged [Re$_6$Q$_8$]$^{2+}$ (Q = S, Se, Te) framework solids, see: Shores, M. P.; Beauvais, L. G.; Long, J. R. *J. Am. Chem. Soc.* **1999**, *121*, 775.

Table 1. Excited-State Parameters for Hexanuclear Rhenium(III) Chalcogenide Clusters in Deoxygenated CH_2Cl_2 at 23 ± 2 °C unless Otherwise Noted

no.	compound	$E_{em}{}^a$ (10³ cm⁻¹)	$\phi_{em}{}^b$	τ_o (µs)	k_r (s⁻¹ 10⁴)	k_{nr} (s⁻¹ 10⁵)	ln k_{nr}
1	$(Bu_4N)_4[Re_6S_8Cl_6]$	13.27	0.031	5.1	0.61	1.90	12.15
2	$(Bu_4N)_4[Re_6S_8Br_6]$	12.85	0.012	3.9	0.31	2.53	12.44
3	$(Bu_4N)_4[Re_6S_8I_6]$	12.50	0.011	2.6	0.42	3.80	12.85
4	$[Re_6S_8(PEt_3)_6]Br_2$	13.90	0.044	10.0	0.44	0.96	11.46
5	$[Re_6Se_8(PEt_3)_6]I_2$	13.70	0.068	10.8	0.63	0.86	11.36
6	$[Re_6S_8(PEt_3)_5Br]Br$	13.53	0.043	7.0	0.61	1.36	11.81
7	*trans*-$[Re_6S_8(PEt_3)_4Br_2]$	13.48	0.008	5.7	0.14	1.74	12.07
8	*cis*-$[Re_6S_8(PEt_3)_4Br_2]$	13.33	0.010	4.8	0.20	2.05	12.23
9	(Bu_4N)-*mer*-$[Re_6S_8(PEt_3)_3Br_3]$	13.04	0.019	4.2	0.46	2.35	12.37
10	*trans*-$[Re_6Se_8(PEt_3)_4I_2]$	13.40	0.037	5.4	0.69	1.80	12.09
11	*cis*-$[Re_6S_8(PEt_3)_4I_2]$	13.30	0.029	6.0	0.48	1.62	11.99
12	$[Re_6Se_8(PEt_3)_5I]I$	13.50	0.085	6.5	1.31	1.41	11.85
13	$(Bu_4N)_4[Re_6S_8(CN)_6]$	13.53	0.039	8.8	0.44	1.10	11.60
14	$(Bu_4N)_4[Re_6Se_8(CN)_6]$	13.79	0.115	11.6	0.99	1.12	11.24
15	$[Re_6Se_8(CH_3CN)_6](SbF_6)_2{}^d$	14.40	0.10	14.8	0.68	0.61	11.01
16	$[Re_6Se_8(pyridine)_6](SbF_6)_2{}^d$	14.50	0.163	14.0	1.23	0.63	11.05
17	$[Re_6Se_8(DMF)_6](SbF_6)_2{}^d$	14.70	0.203	18.9	1.07	0.42	10.64
18	$[Re_6Se_8(DMSO)_6](SbF_6)_2{}^d$	15.10	0.238	22.4	1.06	0.34	10.43
19	*trans*-$[Re_6Se_8(PEt_3)_4(CN)_2]$	13.65	0.093	11.6	0.80	0.80	11.27
20	$[Re_6Se_8(PEt_3)_5CN]BPh_4$	13.64	0.022	13.0	0.18	0.78	11.26
21	*trans*-$[Re_6Se_8(PEt_3)_4(CH_3CN)_2](SbF_6)_2{}^c$	13.90	0.035	12.0	0.29	0.80	11.30
22	$[Re_6Se_8(PEt_3)_5(CH_3CN)]SbF_6{}^c$	13.77	0.041	11.6	0.35	0.83	11.32
23	*cis*-$[Re_6Se_8(PEt_3)_4(DMSO)_2](SbF_6)_2{}^c$	13.87	0.069	12.7	0.54	0.73	11.20
24	$[Re_{12}Se_{16}(PEt_3)_{10}(4,4'\text{-bipyridine})](SbF_6)_4[CH_2Cl_2]$	13.70	0.051	6.1	0.84	1.56	11.95

[a] Corrected emission energy maximum. [b] Error in quantum yield measurements is ±10%; absorbance of all solutions was ≤ 0.1. [c] Photophysical measurements performed in solutions containing the axial ligand in excess. [d] Photophysical measurements performed in neat solutions of the axial ligand.
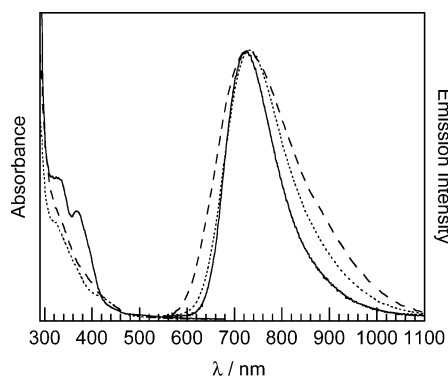

Figure 3. Electronic absorption and emission ($\lambda_{exc} = 435.8$ nm) spectra of $[Re_6S_8(PEt_3)_{6-n}Br_n]^{(2-n)+}$ clusters **4** ($n = 0$, ——), **7** ($n = 2$, trans, - - -) and **9** ($n = 3$, mer, − − −) in dichloromethane. Spectra have been normalized in intensity for clarity.

for **24** $[Re_6Q_8L_6]^z$ clusters. E_{em} decreases along the series Cl > Br > I. S/Se variation of the face-bridging ligands about the Re_6 core does not significantly affect E_{em}, as illustrated by cluster pairs **4/5** (see Figure 2), **13/14**, and **6/12**. Moreover, E_{em} is insensitive to the clusters' local symmetry. However, the emission bandwidth is perturbed, as seen by comparing the emission profiles of O_h-symmetric **4** with those of asymmetric clusters **7** and **9** (Figure 3).

Figure 4 shows the temperature-dependent emission band profile of **1**. There appear to be two emitting states at the highest temperatures; this is most easily seen in the 290 K emission profile, which may be deconvoluted with two Gaussian bands (Supporting Information, Figure S1). The clusters do not alter structure with temperature, therefore the emission temperature dependence is not due to a phase transition.[34] As the temperature is lowered, emission from the low-energy state diminishes, and

(34) Baudron, S. A.; Deluzet, A.; Boubekeur, K.; Batail, P. *Chem. Commun.* **2002**, 2124.
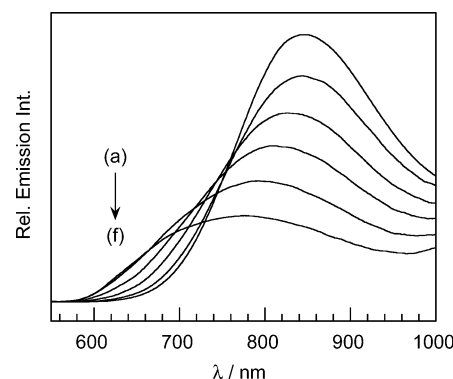

Figure 4. Steady-state emission spectra of **1** at T = (a) 30, (b) 70, (c) 120, (d) 170, (e) 230, and (f) 290 K.

at $T < 240$ K, emission from the higher-energy state dominates. Intersection of the emission spectra at an isosbestic point as the temperature is lowered (~120−150 K) supports this observation. Although other clusters do not clearly exhibit an additional band, an isosbestic point also develops for $T < 150$ K.

The emission band of all clusters remains broad and structureless, even at 10 K. A substantial blue shift and band broadening occurs as temperature rises. This behavior indicates an increased population of higher-energy vibrational states at warmer temperatures. In this series of compounds, the emission band shape is approximately Gaussian. For a Gaussian absorption or emission band, the full width at half-maximum (fwhm) is conveniently quantitated by the band's second central moment, $\bar{m}_2$, given by[35]

$$\bar{m}_2 = \frac{(\text{fwhm})^2}{8 \ln 2} \quad (1)$$

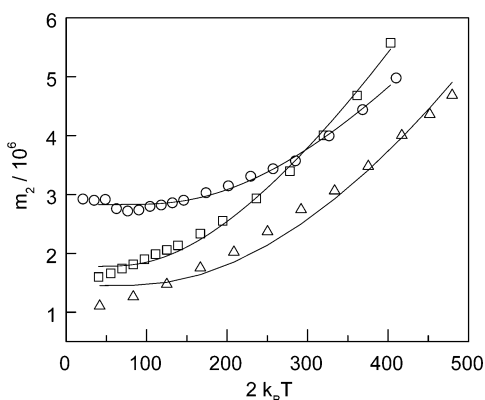Figure 5 demonstrates the behavior of $\bar{m}_2$ for emission from

Figure 5. Second central moments of the emission profiles plotted as a function of temperature for **1** (○), **2** (□), and **3** (△). The solid curves are fit using eq 6.
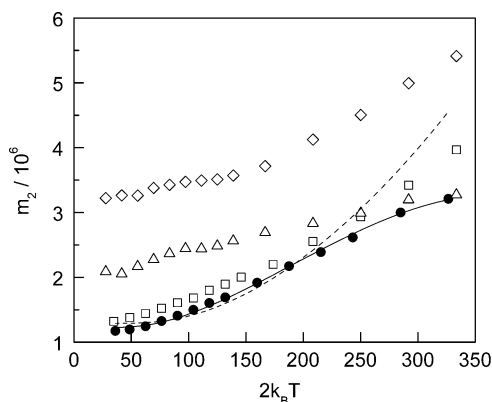

Figure 6. Second central moment of the emission profiles plotted as a function of temperature for $[Re_6S_8(PEt_3)_{6-n}Br_n]^{(2-n)+}$ clusters **6** ($n = 1$, ●), **7** ($n = 2$, trans, △), **8** ($n = 2$, cis, □), and **9** ($n = 3$, mer, ◇). The dashed curve is fit to the second moment of **6** using eq 6; the solid curve is fit to the second moment of **6** using eq 7.

clusters **1**−**3**. In each of the plots, $\bar{m}_2$ increases gradually at very low temperatures and approaches an asymptote at high temperatures. The increase results from populating higher-energy vibrational states and from the accessibility of more normal modes at higher temperature. Therefore, it was quite surprising that the variation in $\bar{m}_2$ with T for most of the remaining $[Re_6Q_8]^{2+}$ compounds examined here deviate from the expected trend. Figure 6 highlights the anomalous behavior for homologous members of the $[Re_6Q_8(PEt_3)_{6-n}X_n]^{(2-n)+}$ series. In a low-temperature regime, typical $\bar{m}_2$ behavior is observed. However, the second moment approaches a constant value with increasing temperatures. In the higher-temperature regime of near-constant bandwidth, the overall emission intensity decreases monotonically. Generally, this anomalous behavior of $\bar{m}_2$ is more pronounced for the selenide clusters. The onset of $\bar{m}_2$ invariance occurs at lower temperature (the inflection point in the $\bar{m}_2$ curves occurs at ~100 K for the selenide clusters as compared to ~170 K for the sulfur clusters).

Electronic Structure Calculations. As with most transition metal complexes, the luminescence of the $[Re_6Q_8]^{2+}$ clusters can be expected to originate from the lowest-energy excited-state manifold. Accordingly, electronic structure calculations were undertaken to determine the nature of the frontier orbitals of the $[Re_6Q_8]^{2+}$ clusters.

Clusters **1**−**3**, **13**, and **14** have been examined theoretically with Hartree−Fock (HF) and density-functional theory (DFT) methods. Geometries were optimized with imposed O_h symmetry, using the effective core potentials and associated double-ζ basis sets of Hay and Wadt.[36,37] Starting geometric parameters were obtained from published crystal structures.[20,38,39] Additional calculations were performed on **1** and **13** with an enhanced basis set, which incorporated polarization (f-orbital) functions on Re and all-electron basis sets on N, C, S, and Cl. Calculated bond lengths and angles are summarized in Table 2 for Hay−Wadt and enhanced basis sets; only HF and Becke3LYP computations were performed with the enhanced basis set. Within the smaller, Hay−Wadt basis set, optimized bond lengths are consistently overestimated. Notably, the average predicted Re−X distances deviate 0.10, 0.16, and 0.12 Å from the observed value for the Hartree−Fock, BLYP, and Becke3LYP methods, respectively. Calculated Re−Re bond lengths are nearer to experiment, with the largest deviation being 0.081 Å for the BLYP functional. The Hartree−Fock and Becke3LYP methods consistently outperform BLYP for metrical predictions of these tetranegative clusters, owing to improper asymptotic decay of the BLYP exchange-correlation functional. The Becke3LYP hybrid functional, which incorporates a percentage of exact exchange, predicts bond lengths that are within 0.02 Å of the average of HF and BLYP results. The internal consistency between experimental metrics and calculated results of the HF and Becke3LYP methods signify the need for exact exchange in geometry optimizations of anionic clusters. For this reason, we discuss only results obtained from HF and Becke3LYP calculations. Geometry optimizations of **1** and **13** were completed using an enhanced basis set that included two additional f-orbital shells on Re and a triple-ζ basis on lighter atoms. Geometries calculated with this larger basis better reproduce crystallographic Re−Re and Re−S bond lengths, but Re−X distances remain overestimated by ~0.1 Å. Notwithstanding, the quality of the calculated geometries is comparable with that of the available calculations on rhenium-containing systems employing effective core potentials[40,41] and all-electron basis sets.[42]

Figure 7 depicts the e_g HOMOs and a_{2g} LUMO, respectively, of the representative cluster $[Re_6S_8Br_6]^{4-}$, derived from Kohn−Sham orbitals within the hybrid Becke3LYP functional and the enhanced basis set. The identity of the frontier orbitals is unaffected by the nature of the apical halide and by changes in basis set. The LUMO is composed exclusively of rhenium d orbitals; s and p orbitals of the Q_8 cube and the Re_6 and X_6 octahedra do not span the A_{2g} representation in O_h.[43] Inclusion of d orbitals in the basis sets for Q and X leaves the LUMO composition unaltered, and within the precision of the calculation, the a_{2g} orbital remains exclusively composed of Re d-functions. The e_g HOMOs are dominated by rhenium $d_{x^2-y^2}$ orbitals, having δ symmetry[44] with respect to the apical ligands;

(35) Markham, J. J. *Rev. Mod. Phys.* **1959**, *31*, 956.

(36) Wadt, W. R.; Hay, P. J. *J. Chem. Phys.* **1985**, *82*, 284.
(37) Wadt, W. R.; Hay, P. J. *J. Chem. Phys.* **1985**, *82*, 299.
(38) Beauvais, L. G.; Shores, M. P.; Long, J. R. *Chem. Mater.* **1998**, *10*, 3783.
(39) Mironov, Y. V.; Cody, J. A.; Albrecht-Schmitt, T. E.; Ibers, J. A. *J. Am. Chem. Soc.* **1997**, *119*, 493.
(40) Köstlmeier, S.; Nauslov, V. A.; Herrmann, W. A.; Rösch, N. *Organometallics* **1997**, *16*, 1786.
(41) Bosque, R.; Maseras, F.; Eisenstein, O.; Patel, B. P.; Yao, W.; Crabtree, R. H. *Inorg. Chem.* **1997**, *36*, 5505.
(42) Cotton, F. A.; Gu, J.; Murillo, C. A.; Timmons, D. J. *J. Chem. Soc., Dalton Trans.* **1999**, 3741.
(43) Cotton, F. A. *Chemical Applications of Group Theory*, 3rd ed.; Wiley-Interscience: New York, 1990.

Table 2. Calculated $[Re_6S_8X_6]^{4-}$ Geometries (X = Cl, Br, I, CN) with Imposed O_h Symmetry, Employing the Hay−Wadt and Enhanced Basis Sets

		Hay−Wadt basis set		
$[Re_6S_8Cl_6]^{4-}$	HF	BLYP	Becke3LYP	experimental[a]
Re−centroid (Å)	1.8442	1.8913	1.8697	
Re−Re (Å)	2.6081	2.6748	2.6442	2.601(4)
Re−S (Å)	2.4880	2.5346	2.5081	2.403(9)
Re−Cl (Å)	2.5401	2.5813	2.5486	2.451(1)
∠S−Re−Cl (deg)	91.980	92.229	92.228	93(1)
$[Re_6S_8Br_6]^{4-}$	HF	BLYP	Becke3LYP	experimental[b]
Re−centroid (Å)	1.8452	1.8918	1.8700	
Re−Re (Å)	2.6070	2.6754	2.6446	2.596(3)
Re−S (Å)	2.4860	2.5325	2.5066	2.397(10)
Re−Br (Å)	2.7087	2.7581	2.7186	2.596(6)
∠S−Re−Br (deg)	92.0	92.3	92.3	93(1)
$[Re_6S_8I_6]^{4-}$	HF	BLYP	Becke3LYP	experimental[c]
Re−centroid (Å)	1.8462	1.8927	1.8705	
Re−Re (Å)	2.6110	2.6767	2.6453	2.607(3)
Re−S (Å)	2.4838	2.5311	2.5038	2.408(11)
Re−I (Å)	2.8930	2.9578	2.9070	2.780(5)
∠S−Re−I (deg)	92.1	92.3	92.3	93.4(2)
$[Re_6S_8(CN)_6]^{4-}$	HF	BLYP	Becke3LYP[d]	experimental[e]
Re−centroid (Å)	1.8450	1.8970		
Re−Re (Å)	2.6092	2.6828		2.602(4)
Re−S (Å)	2.4928	2.5430		2.413(9)
Re−C (Å)	2.1168	2.1042		2.122(9)
C−N (Å)	1.1667	1.2093		1.16
∠S−Re−C (deg)	91.9	92.2		93(4)
$[Re_6Se_8(CN)_6]^{4-}$	HF	BLYP	Becke3LYP	experimental[f]
Re−centroid (Å)	1.868	1.918	1.896	
Re−Re (Å)	2.641	2.754	2.681	2.633(1)
Re−Se (Å)	2.581	2.636	2.606	2.533(5)
Re−C (Å)	2.121	2.104	2.097	2.09(1)
C−N (Å)	1.168	1.211	1.197	1.164(5)
∠Se−Re−C (deg)	90.9	91.2	91.2	92(2)
		enhanced basis set		
$[Re_6S_8Cl_6]^{4-}$	HF		Becke3LYP	experimental[a]
Re−centroid (Å)	1.797		1.837	
Re−Re (Å)	2.541		2.597	2.601(4)
Re−S (Å)	2.414		2.435	2.403(9)
Re−Cl (Å)	2.567		2.555	2.451(1)
∠S−Re−Cl (deg)	87.83		92.75	93(1)
$[Re_6S_8(CN)_6]^{4-\ e}$	HF		Becke3LYP	experimental[d]
Re−centroid (Å)	1.804		1.885	
Re−Re (Å)	2.550		2.608	2.602(4)
Re−S (Å)	2.425		2.445	2.413(9)
Re−C (Å)	2.172		2.133	2.122(9)
C−N (Å)	1.143		1.166	1.16
∠S−Re−C (deg)				93(4)

[a] From $(Bu_4N)_4[Re_6S_8Cl_6]$ (ref 20). [b] From $Cs_4[Re_6S_8Br_6] \cdot CsBr$ (ref 20). [c] From $Cs_4[Re_6S_8I_6] \cdot 2CsI$ (ref 20). [d] The Becke3LYP/LANL2DZ geometry optimization of this cluster failed to converge to an energy minimum. [e] From $NaCs_3[Re_6S_8(CN)_6]$ (ref 38). [f] From $(Me_4N)_4[Re_6Se_8(CN)_6] \cdot 3^1/_3H_2O$ (ref 39).

these HOMOs are confined to the cubic faces of the cluster. This finding differs from results of previous Xα calculations, which indicate halide-dominated HOMOs.[45,46] Orbital energies and percentage contributions from the Re_6 octahedron, the Q_8 cube, and the exopolyhedral X_6 for clusters **1**−**3** and **13**, using Hay−Wadt effective core potentials and basis are listed in the Supporting Information (Tables S1−S4). Results of extended Hückel calculations are included for comparison.[47,48] The apportioning scheme is that of Mulliken;[49] the HOMO composi-

tion is computed to be 65−73% Re, 27−35% Q, and 1−3% axial ligand, and the LUMO is 100% composed of Re. Within the same theoretical method, e_g HOMO compositions vary not more than 2.5% with changes in X for halide clusters. The ordering of nonfrontier orbitals is irregular, with numerous near-degeneracies occurring. In the case of **13**, the BLYP calculation indicates a t_{1g} LUMO which lies 0.05 eV beneath the a_{2g} LUMO counterpart of **1**−**3**; the extended Hückel calculation indicates an a_{1g} HOMO 0.04 eV above the e_g orbitals that are HOMOs of **1**−**3**. We believe these irregularities to be artifacts of the small energy differences with the a_{2g} and e_g orbitals that are in all other cases the frontier orbitals.

(44) Cotton, F. A.; Nocera, D. G. *Acc. Chem. Res.* **2000**, *33*, 483.
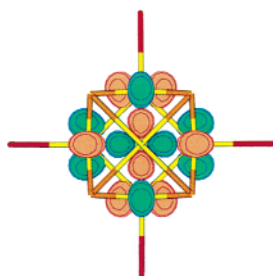(45) Arratia-Pérez, R.; Hernández-Acevedo, L. *J. Chem. Phys.* **1999**, *110*, 2529.
(46) Arratia-Pérez, R.; Hernández-Acevedo, L. *J. Chem. Phys.* **1999**, *111*, 168.
(47) Hoffmann, R. *J. Chem. Phys.* **1963**, *39*, 1397.
(48) Stowasser, R.; Hoffmann, R. *J. Am. Chem. Soc.* **1999**, *121*, 3414.

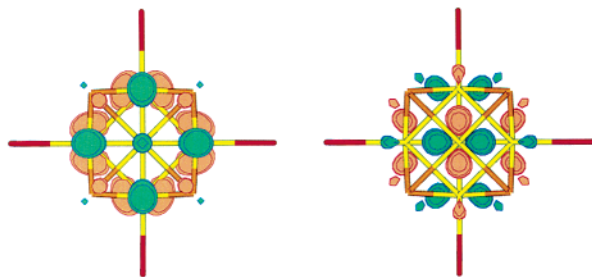(49) Mulliken, R. S. *J. Chem. Phys.* **1955**, *23*, 1833.

LUMO

HOMO

Figure 7. Degenerate e_g HOMOs and a_{2g} LUMO of **2** calculated at the Becke3LYP/LANL2DZ level of theory. The orbitals calculated by HF or BLYP, within the same basis set, are strictly analogous.

The HOMO–LUMO gap (and hence the hardness)[50,51] varies widely according to the level of theory. If experimental emission energies approximate the HOMO–LUMO energy difference, all methods would suggest that the emission energy changes not more than 7% upon interchanging the six halides (**1**–**3**); the experimental range is 6%.[52] Such an approximation is tenuous, however, without accurate, spin-unrestricted calculations of the triplet state. Orbitals within ∼1 eV of the frontier levels have variable metal character, ranging from 6 to 84%. Occupied orbitals near the e_g HOMO (but not the HOMO itself) bear substantial amplitude on the apical ligands.

Photophysical Properties of [Re₆Q₈]²⁺ Clusters. Fluid-solution emission quantum yields (ϕ_{em}) and lifetimes (τ_o) of the 24 $[Re_6Q_8]^{2+}$ clusters are listed in Table 1. Such long-lived emission suggests luminescence to arise from a symmetry- and spin-forbidden transition. Emission quenching by molecular oxygen confirms an excited state with primarily triplet character. From the measured values of ϕ_{em} and τ_o, in deoxygenated solution, the radiative and nonradiative rate constants, k_r and k_{nr}, are available for each of the clusters according to

$$\phi_{em} = \frac{k_r}{k_{nr} + k_r} = k_r\tau_o \qquad (2)$$

Radiative rate constants of the entire series of $[Re_6Q_8]^{2+}$ clusters fall within 1 order of magnitude ($k_r \approx 10^3$ s^{-1}) of one another. The nonradiative decay rate constants are 1–2 orders of magnitude larger ($k_{nr} \approx 10^5$ s^{-1}) and are more variable across the cluster series. Notably, the k_{nr} values for the $[Re_6Q_8]^{2+}$ compounds are larger than those previously reported for the

(50) Pearson, R. G. *Proc. Natl. Acad. Sci. U.S.A.* **1986**, *83*, 8440.
(51) Pearson, R. G. *Acc. Chem. Res.* **1993**, *26*, 250.
(52) The Xα calculations of refs 45 and 46 indicate that the HOMO–LUMO gap of **1** nearly triples that of **3**.

$[M_6X_{14}]^{2-}$ clusters ($k_{nr} \approx 10^3$ and 10^4 s^{-1}, for Mo₆ and W₆, respectively),[21,53] whereas k_r is similar among the three (Mo₆, W₆, and Re₆) cluster cores.

The temperature dependence of the $[Re_6Q_8]^{2+}$ cluster excited-state properties in the solid state was also investigated. Table 3 collects emission quantum yields and lifetimes for clusters **1**–**14** at both 295 and 75 K. Small changes in these data occur for clusters in solution and in solid phases at room temperature. Solution-phase emission maxima generally shift to higher energy, by only ∼300 cm^{-1}, relative to that observed in the solid state, and excited-state lifetimes shorten and emission quantum yields increase slightly. Temperature, however, markedly influences the photophysical properties of the cluster series. The emission maxima listed in Table 3 red shift, often by 10^3 cm^{-1}, as the temperature is lowered from 295 to 75 K; both ϕ_{em} and τ_o roughly double. Derivation of k_r and k_{nr} show that k_r is largely temperature-independent throughout this range, whereas k_{nr} decreases significantly as the temperature is lowered to 75 K. Hence, changes in k_{nr} primarily govern ϕ_{em}.

Raman Spectroscopy and Frequency Calculations of [Re₆Q₈]²⁺ Clusters. Even the most cursory treatments of k_{nr} identify the normal modes of vibration as gateways for passage from the excited state to the ground state. Raman studies were therefore undertaken to determine the vibrational properties of the $[Re_6Q_8]^{2+}$ clusters. A few extended solids containing the $[Re_6(\mu_3\text{-}S)_8]^{2+}$ core have been examined by Raman spectroscopy,[54] as has an ill-characterized $[Re_6(\mu_3\text{-}S)_4(\mu_3\text{-}Cl)_4Cl_4]$ species.[55] The measurements described here are the first for molecular $[Re_6Q_8]^{2+}$ entities.

Figure 8 shows Raman spectra of the O_h-symmetric halide clusters **1**–**3** measured as crystalline solids using $\lambda_{exc} = 785$ nm. Ten Raman-active fundamentals ($3A_{1g} + 3E_g + 4T_{2g}$) occur for molecular $[Re_6Q_8]^{2+}$ clusters in O_h symmetry. At least eight of the ten Raman lines are observed in the spectrum of **1**, with fewer observable in **2** and **3**. Depolarization experiments identify symmetric modes where the depolarization ratio, ρ, equals the ratio of the scattering intensity for bands produced by perpendicular ($\perp$) to parallel ($\parallel$) polarized excitation light.[56,57] Figure 9 displays the $\perp$ and $\parallel$ Raman spectra of **1**. Nontotally symmetric modes display a value of $\rho = {}^3/_4$ and totally symmetric modes display $0 < \rho < {}^3/_4$. Three polarized Raman fundamentals ($\rho \approx 0$) are identifiable at 222, 304, and 428 cm^{-1}. Halide-based X_6 breathing modes are apparent from their X-dependence (222, 151, and 105 cm^{-1} for **1**, **2**, and **3**, respectively; see Figure 8). The intense, polarized feature at 428–430 cm^{-1} in the Raman spectra of all three clusters is assigned as the A_{1g}-symmetric S_8 breathing mode; this assignment is also based on the band's absence in Raman spectra of the selenide clusters. The Re₆ breathing vibration appears as a weak, polarized peak at 306 cm^{-1}. Its low intensity concurs with published[58] observations in isoelectronic $[Mo_6X_8]^{4+}$ and $[W_6X_8]^{4+}$ clusters, for which the A_{1g} metal-core breathing bands are quite weak.

(53) Zietlow, T. C.; Nocera, D. G.; Gray, H. B. *Inorg. Chem.* **1986**, *25*, 1351.
(54) Lutz, H. D.; Muller, B.; Bronger, W.; Loevenich, M. *J. Alloys Compd.* **1993**, *190*, 181.
(55) Fedorov, V. E.; Mischenko, A. V.; Kolesov, B. A.; Gubin, S. P.; Slovokhotov, Y. L.; Struchkov, Y. T. *Soviet J. Coord. Chem.* **1985**, *11*, 980.
(56) Strommen, D. P. *J. Chem. Educ.* **1992**, *69*, 803.
(57) Dawson, P. *Spectrochim. Acta* **1972**, *28A*, 715.
(58) Schoonover, J. R.; Zeitlow, T. C.; Clark, D. L.; Heppert, J. A.; Chisholm, M. H.; Gray, H. B.; Sattelberger, A. P.; Woodruff, W. P. *Inorg. Chem.* **1996**, *35*, 6606.

Table 3. Variable-Temperature Excited-State Parameters for Hexanuclear Rhenium(III) Clusters Measured in the Solid State[a]

no.	compound	E_{em}^{295K} (10^3 cm^{-1})	E_{em}^{75K} (10^3 cm^{-1})	$\phi_{em}^{295K b}$	ϕ_{em}^{75K}	k_r^{295K} (10^3 s^{-1})	k_r^{75K} (10^3 s^{-1})	k_{nr}^{295K} (10^5 s^{-1})	k_{nr}^{75K} (10^5 s^{-1})	τ_o^{295K} (μs)	τ_o^{75K} (μs)
1	(Bu$_4$N)$_4$ [Re$_6$S$_8$Cl$_6$]	13.03	11.90	0.027	0.051	3.96	3.97	1.41	0.73	6.90	12.9
2	(Bu$_4$N)$_4$ [Re$_6$S$_8$Br$_6$]	12.83	11.63	0.007	0.014	1.70	1.60	2.57	1.00	9.52	3.86
3	(Bu$_4$N)$_4$ [Re$_6$S$_8$I$_6$]	12.20	11.00	0.003	0.008	1.23	0.95	3.97	1.20	2.51	8.26
4	[Re$_6$S$_8$(PEt$_3$)$_6$]Br$_2$	13.77	13.50	0.038	0.085	4.35	1.72	1.11	0.19	8.93	35.7
5	[Re$_6$Se$_8$(PEt$_3$)$_6$]I$_2$	13.43	13.40	0.046	0.124	4.78	5.23	0.98	0.37	9.71	23.8
6	[Re$_6$S$_8$(PEt$_3$)$_5$Br]Br	13.30	12.17	0.013	0.038	1.34	1.60	1.02	0.40	6.94	18.2
7	*trans*-[Re$_6$S$_8$(PEt$_3$)$_4$Br$_2$]	13.50	12.90	0.008	0.201	1.09	0.81	1.43	0.40	6.94	25.0
8	*cis*-[Re$_6$S$_8$(PEt$_3$)$_4$Br$_2$]	13.10	12.17	0.013	0.030	2.27	2.13	1.75	0.70	5.65	13.9
9	(Bu$_4$N)*mer*-[Re$_6$S$_8$(PEt$_3$)$_3$Br$_3$]	12.70	12.00	0.012	0.020	3.50	2.88	2.93	1.42	6.90	3.37
10	*trans*-[Re$_6$Se$_8$(PEt$_3$)$_4$I$_2$]	13.40	12.50	0.018	0.044	2.88	3.14	1.57	0.68	6.25	14.1
11	*cis*-[Re$_6$Se$_8$(PEt$_3$)$_4$I$_2$]	13.20	12.20	0.008	0.016	1.64	1.63	2.12	1.01	4.69	9.71
12	[Re$_6$Se$_8$(PEt$_3$)$_5$I]I	13.30	12.90	0.031	0.126	4.10	7.59	1.28	0.53	7.58	16.7
13	(Bu$_4$N)$_4$[Re$_6$S$_8$(CN)$_6$]	13.40	12.71	0.021	0.034	3.68	2.02	1.68	0.57	5.85	16.9
14	(Bu$_4$N)$_4$[Re$_6$Se$_8$(CN)$_6$]	13.57	12.40	0.049	0.098	3.48	5.19	0.67	0.48	14.1	18.8

[a] E_{em} is the corrected emission energy maximum, ϕ_{em} the quantum yield for emission, k_r the radiative decay rate, k_{nr} the nonradiative decay rate, and τ_o the observed luminescence lifetime. [b] Error in solid-state quantum yield measurements is $\pm$ 25%.
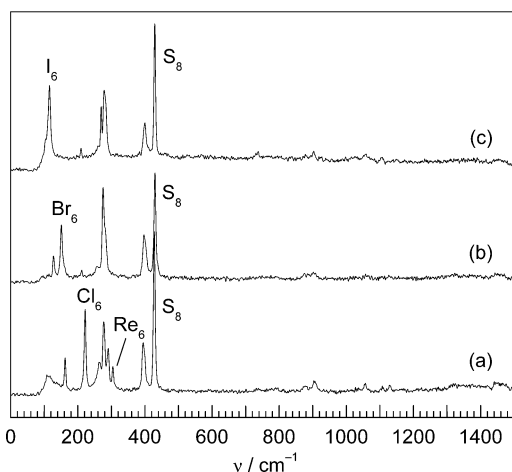

Figure 8. Raman spectra of the [Re$_6$S$_8$X$_6$]$^{2-}$ halide clusters (a) **1**, (b) **2**, and (c) **3**. No vibrational bands are observed above 1000 cm^{-1}.
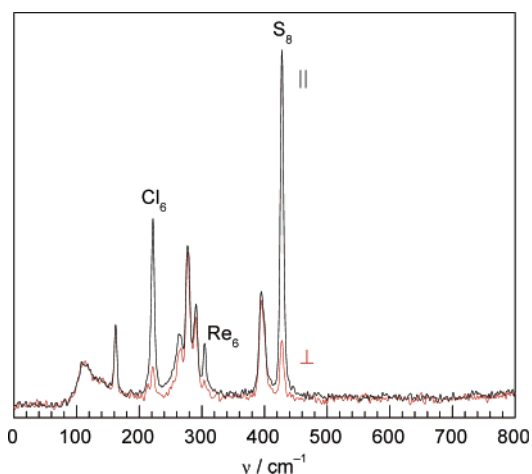

Figure 9. Raman spectra of crystalline **1** where polarization of scattered light is parallel (∥) and perpendicular (⊥) to the incident irradiation. The excitation wavelength was 785 nm. No vibrational bands are observed above 800 cm^{-1}.

Force constant calculations of clusters **1**−**3** aid in the assignment of Raman spectra. It has been previously noted[59] that frequency calculations should be accompanied by peak intensity calculations for both infrared and Raman spectra for

(59) Hess, B. A., Jr.; Schaad, L. J.; Cárscy, P.; Zahrdadník, R. *Chem. Rev.* **1986**, *86*, 709.

Table 4. Observed and Calculated Vibrational Frequencies (cm^{-1}) of [Re$_6$S$_8$Cl$_6$]$^{4-}$ (**1**) Using the Hay−Wadt Effective-Core Potentials and the Associated Basis Set[c]

mode	Hartree–Fock	BLYP	Becke3LYP	experimental[a]
T$_{2u}$	85.78	75.32	79.17	
T$_{2g}$	**100.12** (4.37)	**86.97** (4.21)	**91.23** (4.26)	not observed[b]
T$_{1u}$	105.35	91.42	95.76	
T$_{1g}$	129.58	112.25	117.59	
E$_g$	**116.64** (3.35)	**145.75** (5.35)	**154.95** (4.73)	**162 m**
T$_{2u}$	185.64	169.02	178.19	
T$_{1u}$	216.93	188.55	200.99	
A$_{1g}$ (Cl$_6$)	**225.99** (16.73)	**190.73** (10.94)	**205.33** (11.28)	**222 vs (p)**
T$_{2g}$	**226.42** (0.94)	**191.52** (0.95)	**203.83** (0.83)	not observed
E$_u$	240.71	207.79	221.73	
T$_{1u}$	221.66	226.66	243.08	
E$_g$	**261.92** (14.47)	**226.39** (7.11)	**242.87** (10.05)	**263 m**
E$_g$	**278.57** (8.08)	**241.82** (4.96)	**258.04** (3.56)	**291 m**
T$_{2g}$	**279.78** (20.23)	**236.52** (13.01)	**253.04** (14.24)	**277 s**
T$_{1g}$	283.73	236.69	254.84	
T$_{2u}$	295.32	245.07	264.49	
T$_{1u}$	324.17	272.61	292.38	
A$_{1g}$ (Re$_6$)	**334.95** (17.19)	**279.39** (7.09)	**301.36** (6.60)	**304 w (p)**
A$_{2u}$	410.58	352.86	376.65	
A$_{1g}$ (S$_8$)	**443.80** (124.51)	**373.14** (94.54)	**398.99** (98.64)	**428 vs (p)**
T$_{2g}$	**445.03** (21.95)	**374.96** (19.50)	**401.49** (20.08)	**395 s**
T$_{1u}$	449.88	380.02	406.15	
RMS dev	27.2	36.8	20.7	
av dev	5.56	−34.2	−15.7	

[a] Results are given for peaks with enough intensity for depolarization ratios to be accurately measured to give $\rho = I_\perp/I_\parallel = 0$. Relative band intensities are indicated as vs = very strong, s = strong, m = medium, and w = weak. Peaks that exhibit total polarization are indicated by (p). [b] Instrumental cutoff was 100 cm^{-1}. [c] Raman-active modes are in bold type; calculated Raman intensities (Å^4 amu^{-1}) are reported per vibration in parentheses.

more reliable assignments. Tables 4−6 compile the observed and calculated harmonic vibrational frequencies and attendant intensities for clusters **1**−**3**. More accurate computed frequencies for **1** using the enhanced basis set are included in the Supporting Information (Table S5) for comparison to the calculations presented here.

Figure 10 shows the three totally symmetric vibrations as predicted by an HF/enhanced basis set calculation on ground-state [Re$_6$S$_8$Cl$_6$]$^{4-}$. Such plots are not significantly different for normal vibrations calculated by density-functional methods, and calculated normal modes of other [Re$_6$S$_8$X$_6$]$^{4-}$ clusters (**2**, **3**, and **13**) are analogous. The calculations indicate that the Re$_6$ and X$_6$ breathing modes are intermixed, coupling to each other to result in pairs of in-phase and out-of-phase normal modes.[60] The in-phase A$_{1g}$ mode (predominantly the X$_6$ breathing motion)

Table 5. Observed and Calculated Vibrational Frequencies (cm^{-1}) of [Re$_6$S$_8$Br$_6$]$^{4-}$ (**2**) Using the Hay−Wadt Effective-Core Potentials and the Associated Basis Set[c]

mode	Hartree−Fock	BLYP	Becke3LYP	experimental[a]
T$_{2u}$	55.51	47.01	50.02	
T$_{2g}$	**62.33** (4.43)	**52.20** (4.54)	**55.53** (4.41)	not observed[b]
T$_{1u}$	67.82	56.58	60.22	
T$_{1g}$	100.19	84.70	89.67	
E$_g$	**123.66** (3.23)	**106.44** (5.41)	**115.16** (4.91)	**128 m**
A$_{1g}$ (Br$_6$)	**144.73** (12.98)	**121.67** (10.80)	**132.45** (10.55)	**151 s** (p)
T$_{1u}$	147.75	125.15	136.51	
T$_{2u}$	177.86	161.67	171.07	
E$_g$	**217.85** (0.04)	**183.49** (0.08)	**198.70** (0.01)	not observed
T$_{2g}$	**224.61** (1.19)	**189.76** (1.16)	**202.19** (1.05)	**212 vw**
E$_u$	242.48	208.15	222.46	
T$_{1u}$	243.44	209.74	224.37	
E$_g$	**271.02** (24.57)	**235.86** (11.02)	**250.08** (12.56)	**275 vs**
T$_{2g}$	**282.20** (19.47)	**237.58** (10.42)	**254.33** (12.16)	
T$_{1g}$	287.70	238.79	257.26	
T$_{2u}$	299.99	247.54	267.36	
A$_{1g}$ (Re$_6$)	**315.04** (20.06)	**256.11** (8.69)	**277.44** (8.16)	not observed
T$_{1u}$	317.36	265.22	284.09	
A$_{2u}$	413.76	355.65	679.08	
A$_{1g}$ (S$_8$)	**444.82** (130.42)	**374.87** (88.86)	**400.22** (93.83)	**430 vs (p)**
T$_{2g}$	**447.36** (18.14)	**377.09** (18.30)	**403.36** (18.05)	**397 s**
T$_{1u}$	452.07	382.12	407.95	
RMS dev	20.8	34.2	19.2	
av dev	10.0	−32.1	−15.7	

[a] Results are given for peaks with enough intensity for depolarization ratios to be accurately measured to give $\rho = I_\perp/I_\parallel = 0$. Relative band intensities are indicated as vs = very strong, s = strong, m = medium, and w = weak. Peaks that exhibit total polarization are indicated by (p). [b] Instrumental cutoff was 100 cm^{-1}. [c] Raman-active modes are in bold type; calculated Raman intensities (Å^4 amu^{-1}) are reported per vibration in parentheses.

Table 6. Observed and Calculated Vibrational Frequencies (cm^{-1}) of [Re$_6$S$_8$I$_6$]$^{4-}$ (**3**) Using the Hay−Wadt Effective-Core Potentials and the Associated Basis Set[c]

mode	Hartree−Fock	BLYP	Becke3LYP	experimental[a]
T$_{2u}$	41.41	34.56	37.12	
T$_{2g}$	**45.91** (5.93)	**37.75** (6.28)	**40.60** (5.93)	not observed[b]
T$_{1u}$	51.50	42.14	45.43	
T$_{1g}$	88.73	73.93	78.89	
E$_g$	**92.39** (3.35)	**77.40** (6.10)	**85.93** (5.46)	not observed[b]
A$_{1g}$ (I$_6$)	**105.52** (15.64)	**86.58** (14.11)	**96.09** (13.04)	**105 (p)**
T$_{1u}$	110.43	91.06	101.74	
T$_{2u}$	175.30	158.93	168.51	
E$_g$	**206.78** (0.12)	**173.40** (0.10)	**187.91** (0.03)	not observed
T$_{2g}$	**223.78** (1.21)	**189.16** (1.17)	**201.72** (1.07)	**215 w**
T$_{1u}$	241.85	206.98	222.04	
E$_u$	244.63	209.04	224.28	
E$_g$	**272.79** (23.91)	**236.82** (11.02)	**251.93** (12.61)	**269 s**
T$_{2g}$	**284.86** (18.76)	**238.97** (7.96)	**256.71** (10.06)	**283 s**
T$_{1g}$	292.22	241.11	260.78	
T$_{2u}$	305.01	250.17	271.36	
A$_{1g}$ (Re$_6$)	**309.42** (18.62)	**250.25** (8.01)	**271.71** (7.39)	not observed
T$_{1u}$	316.44	264.49	283.78	
A$_{2u}$	416.24	357.57	382.06	
A$_{1g}$ (S$_8$)	**445.60** (140.08)	**376.24** (80.02)	**402.52** (85.63)	**429 vs (p)**
T$_{2g}$	**449.40** (15.03)	**378.62** (18.49)	**405.99** (17.09)	**401 m**
T$_{1u}$	453.86	383.57	410.47	
RMS dev	21.3	34.8	18.1	
av dev	16.0	−32.6	−14.5	

[a] Results are given for peaks with enough intensity for depolarization ratios to be accurately measured to give $\rho = I_\perp/I_\parallel = 0$. Relative band intensities are indicated as vs = very strong, s = strong, m = medium, and w = weak. Peaks that exhibit total polarization are indicated by (p). [b] Instrumental cutoff was 100 cm^{-1}. [c] Raman-active modes are in bold type; calculated Raman intensities (Å^4 amu^{-1}) are reported per vibration in parentheses.

causes a large polarizability change and an intense Raman band. The out-of-phase A$_{1g}$ mode (predominantly the Re$_6$ breathing motion) is a very weak band resulting from a small change in
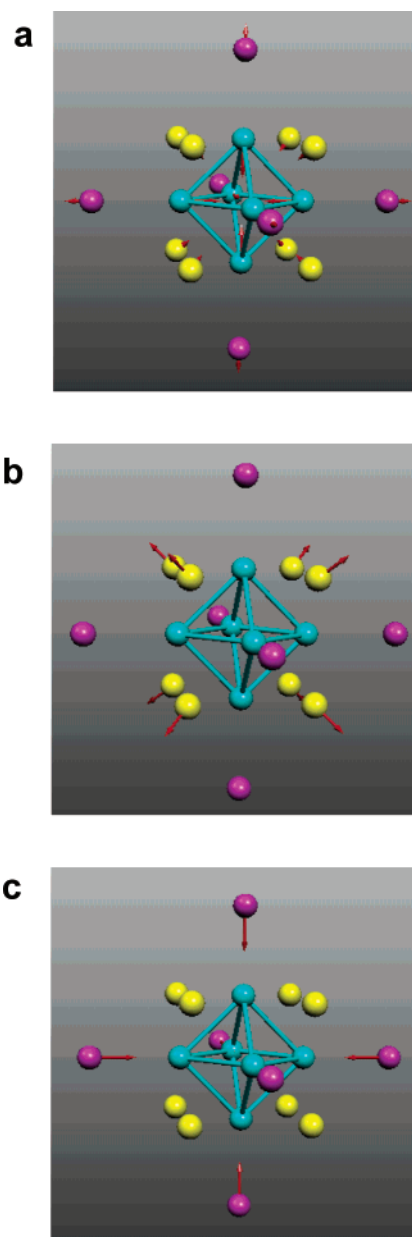

Figure 10. Totally symmetric vibrational modes (a) $\nu_{a_{1g}}$(Re$_6$), (b) $\nu_{a_{1g}}$(S$_8$), and (c) $\nu_{a_{1g}}$(Cl$_6$) of [Re$_6$S$_8$Cl$_6$]$^{4-}$. Vibrations b and c are calculated and observed to be intensely scattering and polarized; vibration a is polarized but calculated and observed to be of weak intensity. Calculations were carried out at the HF/enhanced basis level of theory.

polarizability. The Q$_8$ totally symmetric breathing vibration remains uncoupled from the other two A$_{1g}$ normal modes and is calculated to be the most intense band in the Raman spectra. Experimental band intensities of the three polarized Raman bands conform to these predictions. The single assigned Re$_6$ A$_{1g}$ breathing mode, at 304 cm^{-1} in **1**, is 6% as intense as the S$_8$ breathing mode, in good agreement with DFT predictions, but roughly half that calculated by the Hartree−Fock approximation. The computed relative intensities of the analogous A$_{1g}$ modes in **2** and **3** are comparable, but no obvious candidate for the Re$_6$ A$_{1g}$ breathing mode is visible in the experimental spectra. A similar circumstance prevails in the Raman spectra of Rb$_4$Re$_6$S$_{13}$ and Cs$_4$Re$_6$S$_{13.5}$, for which Re$_6$ breathing modes were not identified.[54]

(60) Hartley, D.; Ware, M. J. *J. Chem. Soc., Chem. Commun.* **1967**, 912.

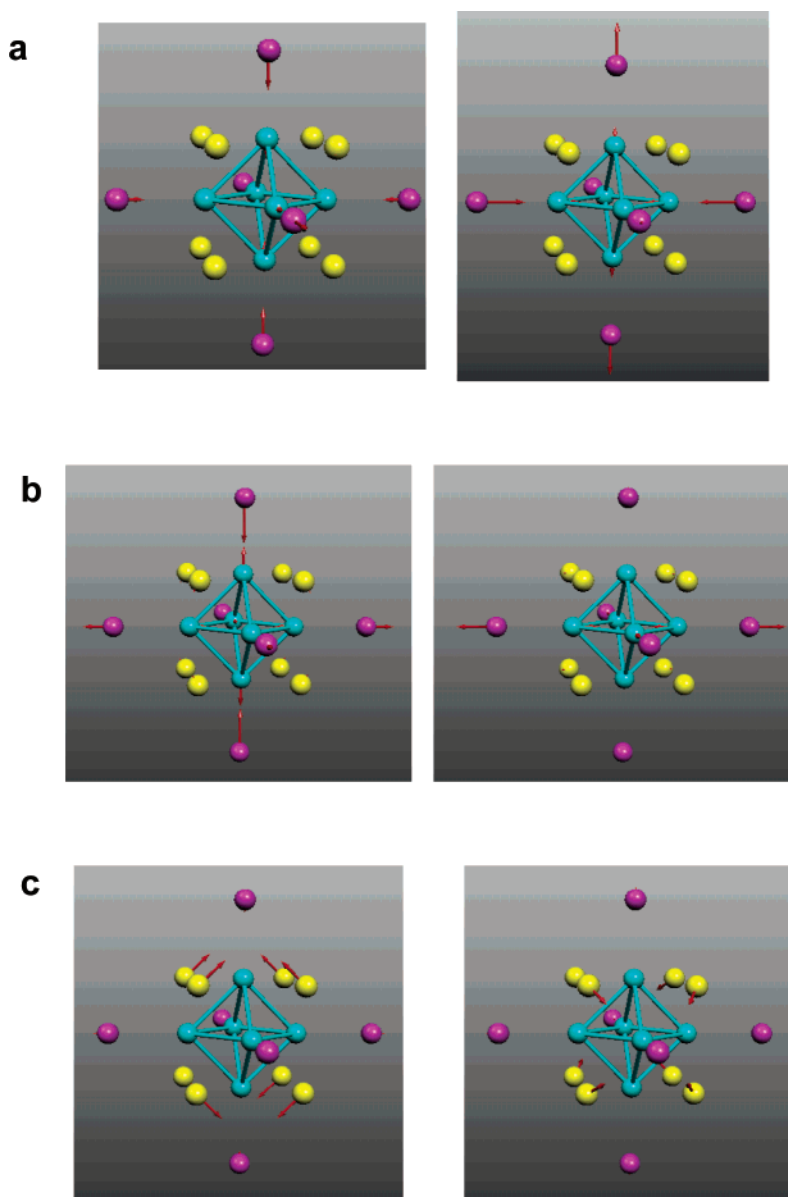**Figure 11.** E_g vibrations of $[Re_6S_8Cl_6]^{4-}$ at (a) 172 cm^{-1} (ν_{e_g}(obsd) = 162 cm^{-1}), (b) 244 cm^{-1} (calculated intensity is small, bands not observed), and (c) 302 cm^{-1} (ν_{e_g}(obsd) = 277 cm^{-1}). Calculated frequencies are those obtained from the HF/enhanced basis level of theory (Supporting Information, Table S5).

Qualitative trends in the calculated Raman intensities aid in assigning nontotally symmetric (T_{2g} and E_g) Raman active modes. Of these, the three sets of E_g vibrations shown in Figure 11 are distinguished by their relevance to excited-state deactivation (vide infra). The majority of E_g and T_{2g} modes are energetically well separated from one another and from the A_{1g} modes; this circumstance facilitates band assignments. A grouping of E_g and T_{2g} modes occurs at 260–290 cm^{-1}; T_{2g} modes are calculated to be more intense than the nearby E_g mode(s) when the intensities are scaled to account for degeneracy (a factor of 2 for E_g modes and factor of 3 for the T_{2g} modes). In the particular case of cluster **2**, an intense resonance at 275 cm^{-1} is fortuitously close to the A_{1g} Re_6 breathing mode, calculated at the Becke3LYP/LANL2DZ level to occur at 277 cm^{-1}. The computed intensity and absence of polarization disqualify this peak as the A_{1g} mode; the more Raman-active E_g mode, calculated at 250 cm^{-1}, is a likelier candidate. Experimental peaks at 397–401 cm^{-1} are assigned as the T_{2g} modes; they occur some 30 cm^{-1} red of the respective A_{1g} S_8

breathing modes. Naïvely, the less intense peaks at 397–401 cm^{-1} might be assigned to the S_8 breathing mode on the basis of the computed frequencies, but the calculated intensities and experimental polarization data prescribe otherwise.

Clusters **4/5** and **13/14** permit direct comparisons of sulfide and selenide clusters. They also illustrate vibrational spectra of clusters possessing axial ligands composed of high-energy oscillators. The three symmetric modes of the phosphine complexes are readily identified upon comparison of the Raman spectra of **4** and **5** shown in Figure 12. Polarized bands at 335 and 105 cm^{-1} in **4** are assigned to the Re_6 and P_6 symmetric breathing vibrations, respectively. The polarized band at 433 cm^{-1} in the spectrum of **4** is replaced by a polarized band of similar intensity at the much lower frequency 195 cm^{-1} in the spectrum of **5**; we assign these vibrations to the Re–Q breathing vibrations. Polarized bands at 631 cm^{-1} are ascribed to symmetric P–C vibrations of the axial ligand. Quantum chemical calculations of phosphine-ligated clusters were not attempted because of their sizes. Force constant calculations
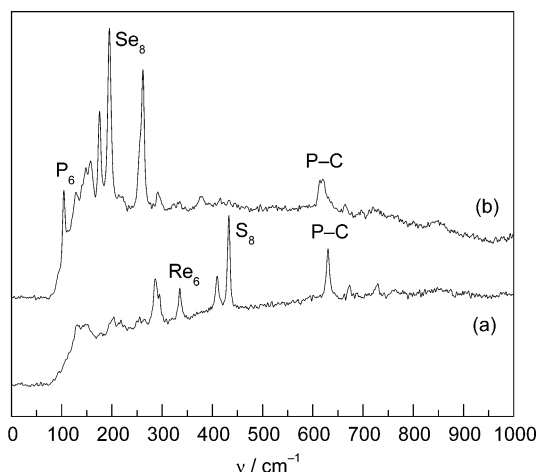
Figure 12. Raman spectra of the $[Re_6Q_8(PEt_3)_6]^{2+}$ (Q = S, Se) clusters (a) **4** and (b) **5**. Vibrational bands above 1000 cm^{-1} are extremely weak and are not shown.

Table 7. Observed and Calculated Vibrational Frequencies (cm^{-1}) of $[Re_6S_8(CN)_6]^{4-}$ (**13**) Using the Hay−Wadt Effective-Core Potentials and the Associated Basis Set[d]

mode	Hartree–Fock	BLYP	experimental[a]
T$_{2u}$	82.52	70.43	
T$_{2g}$	**94.31** (12.97)	**80.44** (15.48)	not observed[b]
T$_{1u}$	96.41	82.42	
T$_{1g}$	110.97	94.35	
T$_{2u}$	174.35	156.65	
E$_g$	**174.38** (6.31)	**149.57** (10.63)	**167**
T$_{2g}$	**222.29** (0.11)	**186.06** (0.07)	**208**
T$_{1u}$	230.15	198.78	
E$_u$	242.78	209.84	
A$_{1g}$ (Re$_6$)	**270.58** (32.54)	**219.57** (26.88)	**245**
E$_g$	**268.83** (15.48)	**236.09** (4.21)	**280**
T$_{2g}$	**283.30** (22.15)	**238.90** (15.60)	**280**
T$_{1g}$	291.08	240.10	
T$_{2u}$	303.42	250.13	
T$_{1u}$	303.63	254.82	
E$_g$	**401.91** (1.42)	**367.77** (5.77)	**368**
T$_{1u}$	405.84	254.82	
A$_{2u}$	407.71	348.09	
A$_{1g}$ (S$_8$)	**416.19** (64.42)	**364.19** (116.29)	**431**
T$_{2g}$	**416.70** (33.37)	**354.62** (24.02)	**417**
T$_{1u}$	421.20	356.65	
T$_{1g}$	429.60	360.22	
T$_{1u}$	443.86	369.87	
A$_{1g}$ (ReC)	**444.42** (49.21)	**381.40** (0.19)	**397**
T$_{1u}$	470.14	391.15	
T$_{2g}$	**478.89** (0.51)	**399.15** (0.24)	not observed
E$_g$	**2355.39** (559.5)	**1997.20** (1210)	**2120**
T$_{1u}$	2355.67	1997.23	
A$_{1g}$ (CN)	**2357.80** (923.5)	**1998.83** (1977)	**2120**
RMS dev[c]	22.8	38.9	
av dev[c]	11.7	32.8	

[a] Results are given for peaks with enough intensity for depolarization ratios to be accurately measured to give $\rho = I_\perp/I_\parallel = 0$. Relative band intensities are indicated as vs = very strong, s = strong, m = medium, and w = weak. Peaks that exhibit total polarization are indicated by (p). [b] Instrumental cutoff was 100 cm^{-1}. [c] Excluding C≡N vibrations. [d] Raman-active modes are in bold type; calculated Raman intensities (Å^4 amu^{-1}) are reported in parentheses.

Table 8. Observed and Calculated Vibrational Frequencies (cm^{-1}) of $[Re_6Se_8(CN)_6]^{4-}$ (**14**) Using the Hay−Wadt Effective-Core Potentials and the Associated Basis Set[d]

mode	Hartree–Fock	BLYP	Becke3LYP	experimental[a]
T$_{2u}$	81.96	70.07	73.98	
T$_{2g}$	**97.53** (9.49)	**82.47** (10.82)	**86.50** (10.21)	not observed[b]
T$_{1u}$	100.20	85.34	88.98	
T$_{1g}$	109.12	92.45	96.47	
T$_{2u}$	137.58	120.86	126.99	
E$_u$	150.39	128.50	137.44	
T$_{2g}$	**156.46** (1.85)	**132.14** (2.23)	**140.49** (1.97)	not observed
E$_g$	**163.39** (13.56)	**137.17** (12.59)	**146.80** (12.33)	not observed
T$_{1u}$	171.40	148.68	158.00	
E$_g$	**172.18** (2.35)	**151.99** (0.01)	**160.78** (0.07)	**195**
T$_{2g}$	**200.60** (23.16)	**168.91** (15.55)	**181.18** (16.26)	**228**
T$_{1g}$	233.12	190.39	206.03	
T$_{1u}$	235.07	193.55	208.39	
A$_{2u}$	242.74	209.30	224.23	
A$_{1g}$ (Re$_6$)	**249.93** (77.41)	**205.89** (30.73)	**221.96** (34.19)	**242**
T$_{2u}$	250.46	210.55	227.23	
A$_{1g}$ (Se$_8$)	**268.79** (14.51)	**223.47** (41.35)	**240.00** (36.11)	**261**
T$_{1u}$	312.13	261.06	280.23	
T$_{2g}$	**316.68** (2.89)	**264.26** (2.65)	**283.88** (3.01)	**288**
E$_g$	**399.70** (0.48)	**369.71** (2.74)	**387.88** (2.19)	not observed
T$_{1u}$	403.18	369.37	388.27	
A$_{1g}$ (ReC)	**420.30** (1.26)	**379.31** (14.68)	**399.19** (9.07)	**397**
T$_{1g}$	443.13	371.29	391.97	
T$_{2u}$	455.02	386.61	406.29	
T$_{1u}$	458.11	385.91	405.98	
T$_{2g}$	**467.59** (12.47)	**393.20** (8.89)	**413.76** (10.30)	not observed
E$_g$	**2339.70** (529.7)	**1988.07** (1060)	**2095.67** (877.6)	**2114**
T$_{1u}$	2339.95	1988.12	2095.77	
A$_{1g}$ (CN)	**2342.25** (788.6)	**1990.13** (1654)	**2097.83** (1345)	**2114**
RMS dev[c]	9.31	38.5	26.5	
av dev[c]	2.9	−36.2	−20.7	

[a] Results are given for peaks with enough intensity for depolarization ratios to be accurately measured to give $\rho = I_\perp/I_\parallel = 0$. Relative band intensities are indicated as vs = very strong, s = strong, m = medium, and w = weak. Peaks that exhibit total polarization are indicated by (p). [b] Instrumental cutoff was 100 cm^{-1}. [c] Excluding C≡N vibrations. [d] Raman-active modes are in bold type; calculated Raman intensities (Å^4 amu^{-1}) are reported in parentheses.

Table 9. Raman Vibrations (cm^{-1}) for Crystalline Hexanuclear Rhenium(III) Chalcogenide Clusters **4**, **6−9**[a]

assigned mode	4	6	7	8	9
		134 m	137 m	128 m	131 m
Re−Br		155 s	156 s	157 s	157 s
Re−P		200 w	191 w	176 w	
	287 s	286 s	285 s	283 s	284 s
Re−Re (Re$_6$) A$_{1g}$	335 m (p)	338 m (p)	335 m (p)	337 m (p)	333 w (p)
	411 s	406 m	406 s	404 s	407 m
Re−S (S$_8$) A$_{1g}$	433 vs (p)	432 vs (p)	430 vs (p)	431 vs (p)	431 vs (p)
P−C	631 s (p)	628 s (p)	632 s (p)	628 s (p)	626 s (p)
	670 w	670 w		670 w	
		701 w			
	729 w	727 w		725 w	727 w
		985 w		980 w	
C−C	1040 w (p)	1041 w (p)	1041 w (p)	1041 w (p)	1041 w (p)

[a] Results are given for peaks with enough intensity for depolarization ratios to be accurately measured to give $\rho = I_\perp/I_\parallel = 0$. Calculations were not available for confirming assignments; only those made from polarization experiments are given. Relative band intensities are indicated as vs = very strong, s = strong, m = medium, and w = weak. Peaks that exhibit total polarization are indicated by (p).

were performed on cyanide clusters **13** and **14**; the experimental and calculated frequencies are listed in Tables 7 and 8. For comparison, frequencies for **13** afforded from calculations using the enhanced basis set are provided in the Supporting Information (Table S6). Depolarization ratios fix the assignment of the A$_{1g}$ modes as 242 cm^{-1} (Re$_6$), 397 cm^{-1} (X$_6$, Re−C), and 2114 cm^{-1} (CN); all three bands appear in the spectra of both

compounds. The 431 and 261 cm^{-1} bands can be assigned to Re−Q (Q = S, Se, respectively).

Symmetry lowering by phosphine substitution increases the number of allowed Raman bands. Table 9 lists the observed bands in the Raman spectrum of the $[Re_6S_8(PEt_3)_{6-n}Br_n]^{(2-n)+}$ clusters **4** ($n = 0$), **6** ($n = 1$), **7** ($n = 2$, trans), **8** ($n = 2$, cis), and **9** ($n = 3$, mer), and assignments are proposed on the basis of comparison; Raman spectra for **6−9** appear in the Supporting

Information (Figures S2−S5). Two polarized bands at ∼335 cm^{-1} and ∼431 cm^{-1} shift little across the series. Band intensities suggest the peak at 335 cm^{-1} to be the Re$_6$ A$_{1g}$-symmetric breathing mode and the 431 cm^{-1} fundamental to be the S$_8$ A$_{1g}$-symmetric breathing mode.

Discussion

Solids and solutions of hexarhenium chalcogenide clusters are red to yellow. These colors result from the low-energy trailing edge of a broad, featureless near-UV absorption band that extends into the visible spectral region. The E_{abs} of this principal absorption tracks the optical electronegativity of the apical ligands of a given [Re$_6$Q$_8$]$^{2+}$ core. As an instructive example, consider the absorption spectra shown in Figure 1 for the [Re$_6$S$_8$X$_6$]$^{4-}$ series, which exhibits a red shift along the series Cl < Br < I. As established by DFT and *ab initio* calculations, orbitals energetically near frontier levels bear substantial apical-ligand character. Promotion of electrons from lower-energy ligand-dominated orbitals to the Re$_6$-based LUMO accounts for the observed trend in E_{abs}. These experimental and theoretical results agree with the original experimental assignment[19] of [Re$_6$S$_8$X$_6$]$^{4-}$ absorption bands as LMCTs, although a better descriptor may be "ligand-to-cluster charge-transfer" transitions.

Intense red to near-infrared luminescence is generated by excitation anywhere into the absorption profile. The trend in emission energies indicates that the emissive state is not LMCT in nature but rather it is associated with the cluster core. With the exclusion of the cluster solvates, E_{em} varies little (<1400 cm^{-1}) across the Re$_6$ series. Electronic structure calculations provide further evidence against an LMCT parentage for Re$_6$ emission. All computational methods suggest the HOMO−LUMO gap to be insensitive to the apical ligands, owing to the dominant metal character of the HOMOs and LUMO. The emission energy supports this theoretical result; E_{em} parallels the HOMO−LUMO gap under the conditions that (a) the e$_g$ HOMOs and a$_{2g}$ LUMO of the ground state correspond to the two singly occupied orbitals in the emitting triplet, (b) their order is unchanged, and (c) changes in the atomic orbital composition of these frontier orbitals upon passing from the ground state to the lowest triplet are minor. Again, with the focus on the [Re$_6$S$_8$X$_6$]$^{4-}$ exemplar, the emission energy is computed to vary negligibly upon halide interchange; a shift of 6% (800 cm^{-1}) is observed in E_{em} across the halides series **1−3**. That a Re$_6$-based triplet excited state is efficiently produced upon LMCT absorption suggests that internal conversion and intersystem crossing are efficient for all clusters.

Although the electronic parentage of the emitting state derives from the same Re$_6$ core, the photophysical properties of [Re$_6$Q$_8$L$_6$]^z compounds vary measurably with the apical ligand L. Most notable is the change in lifetime and quantum yield with L. Given eq 2, the differences in the lifetime and quantum yield arise chiefly from variations in k_{nr} and not k_r (Tables 1 and 3). Thus, the subject of excited-state relaxation in the Re$_6$Q$_8$ clusters is one of thermal energy disposal.

Nonradiative decay occurs by an electronic transition from the thermally equilibrated excited state to isoenergetic, vibrationally excited levels of the ground state followed by vibrational cooling. The efficiency of this transition depends on the vibrational wave function overlap between the ground and excited states. As for any Franck−Condon problem of this type,

the vibrational overlap depends on the excited-state displacement relative to the ground state along an effective nuclear coordinate (typically a critical normal mode of vibration), the energy gap between ground and excited states, and the energies of the excited-state and ground-state vibrational modes. In the limits of a large energy separation between ground and excited states, and of a small difference in equilibrium geometry (i.e., the weak coupling limit), k_{nr} is related to the parameters governing Franck−Condon overlap by[61−63]

$$\ln k_{nr} = (\ln \beta - G) - \frac{\gamma E_{em}}{\hbar \omega_M} \quad (3)$$

where ln β incorporates the nuclear momentum matrix element that couples the excited vibrational state to the ground vibrational state, ω_M is the vibrational frequency that dissipates the excited-state energy (called the accepting mode), and

$$\gamma = \ln\left(\frac{E_{em}}{S\hbar\omega}\right) - 1 \quad (4)$$

In this form of the energy gap law, G represents the phonon coupling strength, defined by the expression

$$G = S(2\bar{n}_j + 1) \quad (5)$$

where $\bar{n}_j = (e^{\hbar\omega_j/kT} - 1)^{-1}$ is the number of vibrations with frequency $\hbar\omega_j$ at thermal equilibrium. Note that in the low-temperature limit β approaches infinity so that $\bar{n}_j \approx 0$ and the expression for G becomes S, where $S \equiv (^1/_2)\sum\Delta Q^2$ is the dimensionless Huang−Rhys parameter that quantifies excited-state distortion. Equation 3 assumes the validity of the weak coupling limit ($\Delta E \gg S\hbar\omega$). The low-temperature limit, requiring $k_B T \ll \hbar\omega$, need not apply to [Re$_6$Q$_8$]$^{2+}$ clusters, so the expression is kept in terms of G. For a series of compounds possessing a common emissive excited-state parentage, variations in G are small, and γ and β vary weakly with ΔE.[64] Under such conditions, eq 3 asserts a linear relationship between ln k_{nr} and ΔE known as the *energy gap law* (EGL).

Figure 13 presents energy gap law plots for clusters **1−24** in fluid solution. Sulfur and selenium clusters both fall on the same line. There is no apparent sensitivity to cluster microsymmetry; partially phosphine-substituted clusters all approach the regression line without distinction. Certain clusters, however, have a definite medium sensitivity. In the case of the iodo cluster **3**, if measurements are made on the pure Bu$_4$N$^+$ salt in neat CH$_2$Cl$_2$, then emission parameters for **3** fall far off-line. This deviation derives mainly from the abbreviated lifetime; the emission quantum yields also drop. If the solution is flooded with excess iodide, the luminescence red shifts some 890 cm^{-1} and the lifetime increases; the cluster rejoins the line, albeit at one end. This behavior is only consistent with ligand lability. Luminescence from hexasolvate clusters **15−18** is also acutely solvent-sensitive. If emission of each cluster is measured in its respective solvent, then luminescence properties fall on the energy gap law best-fit line. When **15−18** are excited in neat CH$_2$Cl$_2$, they emit dimly and with much shortened lifetimes. A

(61) Caspar, J. V.; Meyer, T. J. *J. Am. Chem. Soc.* **1983**, *105*, 5583.
(62) Caspar, J. V.; Kober, E. M.; Sullivan, B. P.; Meyer, T. J. *J. Am. Chem. Soc.* **1982**, *104*, 630.
(63) Meyer, T. J. *Prog. Inorg. Chem.* **1983**, *30*, 389.
(64) Caspar, J. V.; Sullivan, B. P.; Kober, E. M.; Meyer, T. J. *Chem. Phys. Lett.* **1982**, *91*, 91.
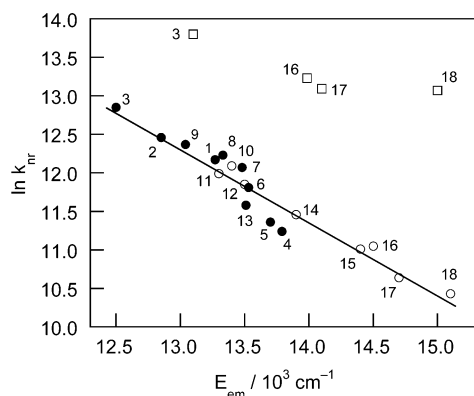
Figure 13. Energy gap law plot constructed from the appropriate data listed in Table 1 for **1**–**18** in CH_2Cl_2 in solution. Filled and open circles indicate the face-bridging sulfur and selenium cluster classes, respectively. The open squares are for data collected on **3** and **15**–**18** dissolved in CH_2Cl_2 solution in the absence of excess ligand. Photophysical measurements of **3** and **15**–**18** that obey the EGL correlation were made for clusters in neat solvents of the axial ligand (**15**–**18**) and for **3** in CH_2Cl_2 containing excess I^-. The linear least-squares line shown is calculated for data depicted with circles (excluding labile clusters in the neat solvents).

recent kinetics study[65] finds that ground-state, thermal solvent exchange in $[Re_6Se_8(PEt_3)_5(solv)]^{2+}$ (solv = MeCN, Me_2SO) cannot account for the ligand lability; the observed photophysical results are therefore consistent with ligand photoexpulsion. In accordance with this contention, EGL behavior persists in the solid state where ligand loss is minimized. Different slopes and intercepts of the EGL fit are observed for solid-phase clusters because of the added solvent reorganization energy affecting both ΔE and k_{nr}.[66,67]

Those clusters in Table 1 having the highest E_{em}, the longest lifetime τ_o, and the largest ϕ_{em} congregate on the lower right-hand extremity of the least-squares line (Figure 13). These compounds, **15**–**18**, all bind N- (acetonitrile, **15**, and pyridine, **16**) or O-donor ligands (DMF, **17**, and DMSO, **18**) in their outer ligand spheres. Together, the data suggest that $[Re_6Q_8]^{2+}$ clusters bound to small, hard donor ligands deliver high-energy emission with maximal quantum yields and lifetimes in the tens of microseconds.[68] Phosphine ligation in $[Re_6Se_8(PEt_3)_6]^{2+}$ (**5**) diminishes the luminescence quantum yield by a third (relative to that of **18**), and the emission characteristics of mixed-ligand entities **6**–**9** and **10**–**12** are similar to those of the respective hexaphosphine clusters **4** and **5**.

An EGL analysis is often informative about the nature of a molecule's emissive excited state. From the linearity of Figure 13, we infer closely similar excited-state electronic structures in the $[Re_6S_8]^{2+}$ and $[Re_6Se_8]^{2+}$ cores and conclude that the $[Re_6Q_8]^{2+}$ lumophore discriminates little among core or apical ligands. Variations in equilibrium bond displacement, ΔQ, and excited-state vibrational frequencies, $\hbar\omega$, must be insignificant relative to the energy gap between the ground and excited state. Systematic changes in k_{nr} can provide valuable information about molecular excited states. To understand these interactions, we have sought to determine the vibrational modes leading to cluster excited-state decay.

Ideally, a Franck–Condon analysis[69–71] on the vibrational fine structure of an emission or absorption band would directly

(65) Gray, T. G.; Holm, R. H. *Inorg. Chem.* **2002**, *41*, 4211.
(66) Chen, P.; Meyer, T. J. *Chem. Rev.* **1998**, *98*, 1439.
(67) Claude, J. P.; Meyer, T. J. *J. Phys. Chem.* **1995**, *99*, 51.
(68) Assuming photoexpulsion of the axial ligands is suppressed.

Table 10. Second Moment Analysis Parameters for Hexanuclear Rhenium(III) Clusters in the Solid State

no.	compound	$\hbar\omega_{eff}{}^a$ (cm^{-1})	$S_{eff}{}^a$	$\hbar\omega_{eff}{}^b$ (cm^{-1})	$S_{eff}{}^b$
1	$(Bu_4N)_4[Re_6S_8Cl_6]$	260	20	220	30
2	$(Bu_4N)_4[Re_6S_8Br_6]$	400	20	330	30
3	$(Bu_4N)_4[Re_6S_8I_6]$	200	20	210	30
4	$[Re_6S_8(PEt_3)_6]Br_2{}^c$	na	na		
5	$[Re_6Se_8(PEt_3)_6]I_2{}^c$	na	na		
6	$[Re_6S_8(PEt_3)_5Br]Br$	230	30	140	50
7	*trans*-$[Re_6S_8(PEt_3)_4Br_2]$	330	10	210	40
8	*cis*-$[Re_6S_8(PEt_3)_4Br_2]$	300	30	160	40
9	(Bu_4N)-*mer*-$[Re_6S_8(PEt_3)_3Br_3]$	340	20	210	30
10	$[Re_6Se_8(PEt_3)_5I]I$	150	40	120	60
11	*trans*-$[Re_6Se_8(PEt_3)_4I_2]$	150	70	130	80
12	*cis*-$[Re_6Se_8(PEt_3)_4I_2]$	150	50	110	70
13	$(Bu_4N)_4[Re_6S_8(CN)_6]$	340	20	220	30
14	$(Bu_4N)_4[Re_6Se_8(CN)_6]$	150	60	110	80

^{a} The effective Huang–Rhys parameter, S_{eff}, and the effective frequency, $\hbar\omega_{eff}$, determined using eq 6. ^{b} The effective Huang–Rhys parameter, S_{eff}, and the effective frequency, $\hbar\omega_{eff}$, determined using eq 7. ^{c} Moment parameters could not be determined, as the band shape displays little or no temperature dependence over the range of temperatures studied.

uncover the vibrations responsible for nonradiative decay. However, the clusters' recalcitrance to exhibiting any vibrational fine structure in the emission spectrum precludes such an analysis. Alternatively, the second moment, deduced from the application of eq 1 to the emission band shape, potentially identifies the vibrational modes responsible for nonradiative decay of the $[Re_6Q_8]^{2+}$ clusters. The normalized second central moment, $\bar{m}_2$, is related to the Huang–Rhys parameter S via G (see eq 5) and relevant vibrational frequency, $\hbar\omega$,[72]

$$\bar{m}_2 = G\,(\hbar\omega)^2\coth\!\left(\frac{1}{2}\beta\hbar\omega\right). \qquad (6)$$

The assumption of a single promoting vibrational mode is not generally valid in large molecules such as the metalloclusters, which can be expected to possess extensive vibrational coupling. In this case, the results given by eq 6 provide an *effective* Huang–Rhys parameter, S_{eff}, and an *effective* vibrational mode, $\hbar\omega_{eff}$,[73] where $S_{eff} = \sum S$ and $\hbar\omega_{eff}$ are given by the weighted average of contributing frequencies ($\hbar\omega_{eff} = \sum S\hbar\omega/\sum S$).

Table 10 contains the values of $\hbar\omega_{eff}$ and S_{eff} obtained from a second moment analysis of the temperature-dependent emission bandwidths of **1**–**14**. Standard analyses[27,32,74] predict that the emission bandwidth increases monotonically with temperature, with a hyperbolic cotangent dependence on $1/T$. Equation 6 accounts for the great majority of experimental data to which it has ever been applied, including three rhenium sulfide clusters, **1**–**3**. However, the remaining hexanuclear rhenium(III) clusters, especially selenide clusters, defy the simple coth law dependence of eq 6; for these, $\bar{m}_2$ versus T plots asymptotically approach a constant emission bandwidth at high temperature. The plots of $\bar{m}_2$ versus T shown in Figure 6 exemplify the aberrant behavior of the nonhalide clusters. This behavior is unusual but not unprecedented,[75–79] and it is typically ignored. The values listed

(69) Ballhausen, C. J. *Molecular Electronic Structures of Transition Metal Complexes*; McGraw-Hill: New York, 1979.
(70) Kober, E. M.; Caspar, J. V.; Lumpkin, R. S.; Meyer, T. J. *J. Am. Chem. Soc.* **1986**, *90*, 3722.
(71) Yersin, H.; Otto, H.; Zink, J. I.; Gliemann, G. *J. Am. Chem. Soc.* **1980**, *102*, 951.
(72) Lax, M. *J. Chem. Phys.* **1952**, *20*, 1752.
(73) Kober, E. M.; Meyer, T. J. *Inorg. Chem.* **1985**, *24*, 106.
(74) Kubo, R.; Toyozawa, Y. *Prog. Theor. Phys.* **1955**, *13*, 160.

in Table 10 were obtained from the application of eq 6 over appropriate low-temperature regimes. Nevertheless, we were interested in exploring various models that might account for the temperature dependence of $[Re_6Q_8]^{2+}$ emission. A multimode variant of eq 6, which assumes either two or three deactivating vibrations, was unsatisfactory, as was another model, where a thermally accessible "dark state" siphons away excited-state energy nonradiatively. We also considered the possibility that the oscillator strength depends on the frequency of the deactivating vibration. For this case, the normalized second central moment is given by the more general expression,[35]

$$\bar{m}_2 = G(\hbar\omega)^2\Big[\coth\Big(\frac{1}{2}\beta\hbar\omega\Big) + \Big(\frac{1}{\Delta\epsilon}\hbar\omega\Big) - \\ \Big(\frac{1}{\Delta\epsilon}\hbar\omega\Big)^2 G \coth^2\Big(\frac{1}{2}\beta\hbar\omega\Big)\Big] \quad (7)$$

where $\Delta\epsilon = \hbar\omega_{abs}$. This equation contains an additional constant and a term proportional to $\coth^2 \beta$. Experimentally, a better correlation between theory and experiment results when the data are fit with eq 7. An example appears in Figure 6 for the moderately deviant cluster **6**. The resulting $\hbar\omega_{eff}$ and S_{eff} calculated from the fit for each cluster **1**−**14** are given in Table 10. Generally, slightly smaller values of $\hbar\omega_{eff}$ are compensated by an increase of S_{eff} when band shapes are analyzed with eq 7 than with eq 6. Clusters **4** and **5** are exceptional due to their invariant $\bar{m}_2$ even up to 345 K; the origin of this insensitivity is unknown. Whichever the model, the values of $\hbar\omega_{eff}$ obtained from the second moment analysis yield the same qualitative result, low-energy vibrational modes that dominate in the deactivation of $[Re_6Q_8]^{2+}$ excited states. The conformity of EGL and second moment analyses further supports this contention. In all cases, substitution of $\hbar\omega_{eff}$ and S_{eff} into the EGL relation of eq 3 yields lines that accord with the experimental data.

Inasmuch as $\hbar\omega_{eff}$ is the weighted average of frequencies, we wished to relate $\hbar\omega_{eff}$ to the specific low-energy modes of the cluster compounds. Group theory-based selection rules[80,81] prescribe that the deactivating vibrational modes of excited $[Re_6Q_8L_6]^z$ species transform as irreducible representations contained in the direct product of the excited-state irreducible representation with itself.[82] Hartree−Fock, density-functional, and extended Hückel calculations indicate a $[core]e_g^3a_{2g}^1$ electron configuration for the emitting triplet, corresponding to a ^3E_g state in O_h symmetry. Hence, vibrational modes with A_{1g}, A_{2g}, and E_g symmetry are relevant to the excited-state decay of the O_h clusters **1**−**3**, **13**, and **14**.[83] Three A_{1g} and six E_g vibrations are present in the $[Re_6Q_8X_6]^{4-}$ (X = Cl, Br, I) octahedral clusters; there are no A_{2g} normal modes. It transpires that the nine potential de-exciting vibrations are Raman active; these modes are shown in Figures 10 and 11. For octahedral

clusters with axial cyanide ligands, two additional E_g modes and an A_{1g} vibration associated with the C≡N moiety occur.

The arithmetic mean of the nine calculated frequencies of the vibrations displayed in Figures 10 and 11 is 257 cm^{-1} (HF/ LANL2DZ), which is near the effective frequency of 260 cm^{-1} determined from the second moment analysis of **1**. Averages of those observable, potentially deactivating Raman frequencies for **2**, **3**, **13**, and **14**, with calculated values used where experimental fundamentals are not detected, also suggest that all nine vibrational modes contribute to the excited-state deactivation. This happenstance might indicate that the apical ligand vibrations dominate nonradiative decay, in contradiction to spectroscopic, computational, and photophysical results, all of which suggest (i) an excited state localized within the $[Re_6Q_8]^{2+}$ core and (ii) an excited-state decay process that proceeds exclusive of vibrational modes involving the apical ligands. It is here that clusters possessing apical cyanide, phosphine, and solvate ligands are informative. In these cases, the axial ligands possess high-energy vibrations. Notwithstanding, introduction of even minor contributions of these high-energy modes to the overall weighted average of $\hbar\omega_{eff}$ causes the second moment and EGL correlation to be at significant variance to the observed results of Table 10 and Figure 13, respectively. Together, these results show that the $[Re_6Q_8]^{2+}$ emitting core is effectively insulated from the high-energy vibrations of the apical ligands.

Concluding Remarks

The principal results and conclusions of this work are as follows:

(a) $[Re_6S_8]^{2+}$ and $[Re_6Se_8]^{2+}$ clusters emit bright red phosphorescence, in the solid state and in solution, upon ultraviolet or blue-light excitation. Those species with oxygen donor ligands deliver maximal quantum yields, the longest lifetimes, and the highest-energy emission. Conversely, clusters having six soft, polarizable ligands, such as iodide, emit with less intensity, shorter lifetimes, and redder luminescence.

(b) Room-temperature luminescence lifetimes of the clusters in fluid solution range from 2 to 22 μs, and quantum yields, from ∼1−24%. Solid-state emission lifetimes and quantum yields, where measured, occupy a similar range at room temperature.

(c) Low-temperature luminescence experiments indicate a progressive red shift of the emission maximum upon cooling, with an increase in the excited-state lifetime and the emission quantum yield.

(d) The long lifetimes, large Stokes shifts, and excited-state quenching by O_2 indicate an emitting excited state with considerable spin-triplet character.

(e) $[Re_6S_8]^{2+}$ and $[Re_6Se_8]^{2+}$ emission obey the approximate energy gap law. This observation implies a common lumophoric kernel in $[Re_6Q_8]^{2+}$ (Q = S, Se) species. It also suggests that these clusters, once excited, share a common deactivation mechanism.

(f) Single-crystal Raman spectroscopy reveals low-frequency ($\leq100-450$ cm^{-1}) modes associated with the $[Re_6Q_8]^{2+}$ core. Polarization measurements identify A_{1g}-symmetric breathing modes; other Raman-active vibrations are assigned by comparison with quantum chemical calculations.

(75) Page, S. E.; Llopis, J. *Appl. Phys.* **1993**, *A57*, 225.
(76) Brasil, M. J.; Motisuke, P.; Decker, F.; Moro, J. R. *J. Phys. C: Solid State Phys.* **1988**, *21*, 3141.
(77) Rice, S. F.; Wilson, R. B.; Solomon, E. I. *Inorg. Chem.* **1980**, *19*, 3425.
(78) Miskowski, V. M.; Smith, T. P.; Loehr, T. M.; Gray, H. B. *J. Am. Chem. Soc.* **1985**, *107*, 7925.
(79) Mikowski, V. M.; Gray, H. B. *Inorg. Chem.* **1987**, *26*, 1108.
(80) Wilson, R. B.; Solomon, E. I. *J. Am. Chem. Soc.* **1980**, *102*, 4085.
(81) Lever, A. B. P.; Solomon, E. I.; Lever, A. B. P. In *Inorganic Electronic Structure and Spectroscopy*; Wiley-Interscience: New York, 1999; Vol. I, Chapter 1.
(82) Bersuker, I. B. *Chem. Rev.* **2001**, *101*, 1067.
(83) Wilson, R. B.; Solomon, E. I. *Inorg. Chem.* **1978**, *17*, 1729.

(g) Analysis of the emission second central moment provides an effective deactivating vibrational frequency, $\hbar\omega_{\text{eff}}$, for individual clusters. The experimental range is $\sim 150-350$ cm^{-1}. This frequency span coincides with the vibrational energies of the $[Re_6Q_8]^{2+}$ subunit, suggesting a core-centered excited state. Quasi-relativistic electronic structure calculations concur with this result; they indicate a lowest-energy excited-state parentage that is largely localized to the cluster core.

(h) Substitution of the second moment derived $\hbar\omega_{\text{eff}}$'s into the approximate energy gap law reproduces the observed photophysical parameters. This observation affirms the validity of the second moment analysis.

(i) Group theory predicts that, for a ^3E_g excited state in O_h symmetry, deactivating vibrations span the A_{1g} and E_g irreducible representations. A normal-mode analysis indicates nine such modes (three A_{1g} and six E_g) that collectively involve the three shells of the cluster structure: the Re_6 octahedron, the Q_8 cube of face-bridging chalcogenides, and the six axial ligands. For clusters containing only low-energy vibrational modes (e.g., $[Re_6S_8X_6]^{4-}$), $\hbar\omega_{\text{eff}}$ comprises roughly equally weighted contributions from all nine candidate modes. Least-squares fits to the energy gap law are not sufficiently sensitive to distinguish among these low-energy modes. This result illustrates inherent limitations of paradigmatic photophysical experimental methods. Specifically, use of the energy gap law to distinguish among low-energy de-exciting vibrations is problematic, and such analyses, when pursued,[66] are sometimes prone to overinterpretation.

(j) Clusters possessing axial phosphine, cyanide, and solvate ligands possess modes of sufficient energy, for energy gap law purposes, to be discernible from other intracluster vibrations. Notwithstanding, these clusters obey the energy gap law correlation, indicating that the emitting excited state is insulated from vibrations within the axial ligands.

The foregoing results constitute the most comprehensive single study of metallocluster-based luminescence to date. The combined spectroscopic, computational, and photophysical studies show that long-lived and bright luminescence may be obtained as long as the $[Re_6Q_8]^{2+}$ core is unperturbed, regardless of the nature of the axial ligand. Consequently, substitution of Q ligands may disable cluster emission, as observed for a limited subclass of compounds in which Q was substituted by a chloride anion.[84] The photophysics of compositionally variant metallic cores have yet to be investigated. Hexanuclear technetium sulfide clusters $[Tc_6S_8]^{2+}$ exist in extended solid phases,[85] and soluble mixed rhenium−osmium derivatives have been reported.[86] For both systems, excited-state properties are uncharted.

The energy gap law correlation establishes that axial substitution at the cluster core affects photophysical properties in a predictable way; consequently, the emissions of $[Re_6S_8]^{2+}$ and $[Re_6Se_8]^{2+}$ are optimizable at the level of *synthesis*. Experimental prospects are many, since the axial ligands enable the chemical modification of a cluster core that effectively is a molecular light bulb. The findings herein offer solid guidance

for future studies and applications relying on the excited-state properties of these remarkable metal−metal bonded species.

Experimental Section

Materials. Hexanuclear rhenium(III) chalcogenide clusters were prepared according to published procedures and gave satisfactory ^1H NMR and ^{31}P NMR (where applicable) spectra and mass spectral analyses.[19−21,87] Spectroscopic-grade solvents (Burdick and Jackson) were used for electronic absorption and emission and photophysical measurements. Solvents were used as received, though care was taken to minimize exposure to moisture. Solutions for spectroscopic experiments were prepared by dissolving an adequate amount of cluster **1−14** in approximately 10 mL of dichloromethane. Clusters **15−18** were dissolved in solvents of their respective axial ligands. In the case of cluster **3**, an excess of $Bu_4N^+I^-$ was dissolved in dichloromethane.

General Methods. Spectroscopic and photophysical measurements of solutions were performed on samples contained within a cell equipped with a 10-mL solvent reservoir and a 1-cm clear fused quartz cell (Starna Cells, Inc.). The two chambers were isolated from each other by a high-vacuum Teflon valve and from the environment with a second high-vacuum Teflon valve. Solvents were vacuum distilled into the solvent chamber. Each solution was freeze−pump−thawed (10^{-6} Torr) three times to expunge O_2, which was observed to quench the long-lived emission of the $[Re_6Q_8]^{2+}$ clusters. Absorption spectra were recorded on an OLIS-modified Cary-17 spectrophotometer.

Steady-State Luminescence Measurements. Steady-state emission spectra of solids and solutions were recorded on a modified high-resolution custom-built spectrometer. An Ushio 200-W Hg−Xe arc lamp (Second Source) mounted in an Oriel 60100 lamp housing (f/4) was focused on the entrance slit of a Spex 1680 double monochromator (0.22 m, f/4). Wavelength-selected 435.8-nm excitation light was collimated by an f/4 fused silica lens and focused with an f/2 fused silica lens onto solid samples positioned at 45° to the excitation beam. The emitted light was collected at 90° to the excitation beam with an f/2 fused silica lens and then focused by an f/8 lens through a Corion colored glass long-pass cutoff filter onto the entrance slit of a Spex 1870B scanning monochromator (f/8). The glass cutoff filters were omitted for the collection of quantum yield data. The dispersed emission was detected by a red-sensitive R316-02 Hamamatsu PMT, cooled to −40 °C in a Products for Research TE241RF housing powered by a Bertan Associates model 215 high voltage power supply. The signal from the PMT was passed through a preamp converting current to potential (EG&G model 181) and into either an EG&G 5209 lock-in amplifier or a Stanford Research Systems SR400 two-channel photon counter. The input signal to both instruments was phase-matched to a reference signal generated by a light chopper placed between the excitation monochromator and the sample chamber. A chopper frequency of 338 Hz was controlled by a Stanford Research Systems SR540 signal generator. The output from the lock-in amplifier is fed through an A/D converter to a computer; the output from the photon counter is fed through a GPIB interface to a computer. Emission spectra were corrected for the wavelength response of the PMT and instrument using an NBS standard lamp. The emission spectrometer was scanned across the width of the emission spectra at a rate of approximately 1 nm/s. Data acquisition was performed with code written using LabView 5.0 software, and all data were analyzed using Origin 6.0.

Emission quantum yields of solubilized clusters (23 ± 2 °C) were determined by referencing sample emission intensities to optically dilute samples ($\epsilon_{435.8 \text{ nm}} \leq 0.1$ M^{-1} cm^{-1}) of $(Bu_4N)_2[Mo_6Cl_{14}]$ in CH$_3$CN ($\phi_{\text{em}} = 0.19$,[88] $\lambda_{\text{exc}} = 436$ nm). Samples were excited with 435.8-nm light, and measured quantum yields were corrected as follows:

(84) Guilbaud, C.; Deluzet, A.; Domercq.; Moliné, P.; Coulon, C.; Boubekeur, K.; Batail, P. *Chem. Commun.* **1999**, 1867.
(85) Bronger, W. In *Metal Clusters in Chemistry*; Braunstein, P., Oro, L. A., Raithby, P. R., Eds.; Wiley: New York, 1999; Vol. 3, p 1591.
(86) Tulsky, E. G.; Long, J. R. *Inorg. Chem.* **2001**, *40*, 6990.

(87) Gray, T. G.; Holm, R. H. *Inorg. Chem.* **2002**, *41*, 4211.
(88) Maverick, A. W.; Najdzionek, J. S.; MacKenzie, D.; Nocera, D. G.; Gray, H. B. *J. Am. Chem. Soc.* **1983**, *105*, 1878.

$$\phi_s = \phi_r \left(\frac{A_r \eta_s^{\,2} D_s}{A_s \eta_r^{\,2} D_r} \right) \qquad (8)$$

where the s and r indices designate the sample and reference samples, respectively, A is the absorbance at λ_{exc}, η is the average refractive index of the appropriate solution, and D is the integrated area under the corrected emission spectrum.

Solid-state quantum yields were obtained using the method of Wrighton et al.;[89] MgO was used as the nonabsorbing standard. To ensure that the same number of photons was incident on the sample and the nonabsorbing standard, the sample holder was aligned by matching the diffuse reflectance of the standard with that of the sample at a wavelength where the sample did not absorb (696.5 nm). Reflectance spectra were obtained by scanning the emission monochromator over the exciting wavelength (435.8 nm) at a rate of approximately 1 nm/s. This process was repeated at low temperatures, using the cryogenic refrigeration system to control the temperature. Corrected reflectance and emission spectra were used to determine the quantum yield of solids as follows:

$$\phi_s = \phi_r \cdot \frac{D_s}{D_r} \left(\frac{R_{MgO} - R_r}{R_{MgO} - R_s} \right) \qquad (9)$$

where D_s and D_r are defined previously, R_{MgO} is the reflectance spectrum intensity of MgO, and R_r and R_s are the reflectance spectrum intensities of sample and reference, which was $(Bu_4N)_2[Mo_6Cl_{14}]$. The average of three successive measurements was used in determining the quantum yields.

Temperature-dependent emission spectra were collected on solid samples under vacuum using a front-face solid sample holder aligned at 45° to the incident beam. Samples were thermally regulated from 15 to 345 K using an Air Products CSA-202E cryogenic refrigeration system equipped with a DMX-1 vacuum shroud interface, a DE-202 expander module, and an Air Products 1R02A air-cooled compressor. Powdered solid samples were compressed into the 5 mm × 5 mm × 2 mm sample well of a machined copper block, which was mounted to the sample head of the DE-202 cryostat thus allowing for reproducible positioning and temperature control. Indium foil is used between the block and the expander to ensure good thermal conductivity. The temperature was varied using a Scientific Instruments 9600-5 temperature controller with a resistive heating element and was monitored using a gold-calomel thermocouple (Advanced Research Systems) situated at the end of the expander module. The DMX-1 vacuum shroud interface has two Suprasil windows on adjacent sides allowing excitation light to strike the sample and emitted light to be collected at 90° to the incident beam. Temperature-dependent data were run in both directions (high to low temperature and low to high) to ensure reproducibility.

Time-Resolved Luminescence Measurements. Time-resolved luminescence data were collected on a nanosecond laser instrument utilizing a Coherent Infinity XPO tunable laser (fwhm = 7 ns) as the source. The Infinity Nd:YAG laser system consisted of an internal diode pumped, Q-switched oscillator, which provided the seed pulse for a dual rod, single lamp, amplified stage. Third harmonic radiation was generated from the Nd:YAG 1064 nm fundamental via Type I polarization and frequency mixing in tuned BBO crystals. The resultant 355-nm beam was passed through a type I tunable XPO to produce an excitation wavelength of 460 nm. Solution and solid sample emission were collected at 90° and 45°, respectively, to the incident excitation beam by an f/4 collimating lens and was passed onto the entrance slit of an Instruments SA Triax 320 monochromator by an f/4 focusing lens. Solid samples were positioned at an oblique angle to the incident beam. The signal wavelengths were dispersed by a grating possessing 300 grooves/cm at a blaze wavelength of 500 nm. A wavelength selected signal between 720 and 750 nm, depending on the emission maximum of the sample, was detected by a Hamamatsu R928 PMT. Decay traces were constructed from signals that were averaged for ~1000 scans by a LeCroy 9384CM 1-GHz digital oscilloscope, which was triggered from the Q-switch sync output of the laser. Monochromator operation, data storage, and data manipulation were managed by National Instruments v4.0 driver software (Labview) incorporated into code written at MIT. Communication between a Dell Optiplex GX-1 computer and the instrumentation was achieved through an IEEE−488 (GPIB) interface. Data were fit using Origin 6.0. Temperature-dependent lifetimes were recorded on samples mounted in the cryostat with the same geometry as that used for recording temperature-dependent emission spectra.

Raman Spectroscopy. Visible Raman spectra were obtained on polycrystalline samples mounted on a Hololab 5000R Modular Research Raman spectrometer, which was housed in the MIT Center for Material Science and Engineering (CMSE) Raman microscopy lab. The exciting beam was focused onto signal crystals with a fiber-optic coupled Leica DMLP optical microscope with a motorized stage (Kasier Optical Systems). The laser source was a Coherent Laser Group Renova 890 CW TiS Laser SW LP; 785-nm sample excitation circumvented high levels of background fluorescence. The detector was a high-resolution CCD camera containing a 2048 × 512 Array Front Illuminated EEV MPP chip. Polycrystalline samples were placed on glass microscope slides and held in place with a glass coverslip. Samples were run using the 10× objective on the microscope. Signal-to-noise was highly dependent on the specific focal point on the sample. Several attempts were often necessary to achieve reasonable data. Acquisitions (5−10) were averaged per sample. The instrument was calibrated to provide Raman shifts (rel cm⁻¹) using CCl_4 as the standard. Instrument alignment was accomplished using the $(Bu_4N)_4[Re_6S_8Cl_6]$ sample, which consistently provided the strongest Raman signal. Depolarization ratios were determined on solid samples by averaging the results from the focused beam at several positions on a single crystal.[90]

Calculations. Spin-restricted Hartree−Fock[91] and density-functional theory (DFT)[92,93] computations were performed within the Gaussian 98 program suite.[94] DFT calculations employed either the Becke nonlocal exchange functional[95] or the Becke three-parameter hybrid exchange functional[96] with the correlation functional of Lee, Yang, and Parr.[97,98] Direct methods were used for self-consistent field convergence. Because of the size of the clusters, relativistic effective core potentials and the standard double-ζ basis sets of Hay and Wadt were utilized for Re, C, N, S, Cl, Br, and I. These potentials incorporate relativistic effects for Re and I. Additionally, a more extensive basis set, termed the "enhanced basis set," was applied to clusters **1** and **2**. This larger basis comprised the 6-311G(d,p) basis set for S, Cl, and Br, and the

(89) Wrighton, M. S.; Ginley, D. S.; Morse, D. L. *J. Phys. Chem.* **1974**, *78*, 2229.

(90) *Raman Microscopy: Developments and Applications*; Turrell, G., Corset, J., Eds.; Harcourt Brace: San Diego, CA, 1996.

(91) Szabo, A.; Ostlund, N. S. *Modern Quantum Chemistry*; Dover: New York, 1996; Chapter 3.

(92) *Chemical Applications of Density-Functional Theory*; Laird, B. B., Ross, R. B., Ziegler, T., Eds.; ACS Symposium Series 629; American Chemical Society: Washington, DC, 1996.

(93) Parr, R. G.; Yang, W. *Density-Functional Theory of Atoms and Molecules*; Oxford: New York, 1989.

(94) Frisch, M. J.; Trucks, G. W.; Schlegel, H. B.; Scuseria, G. E.; Robb, M. A.; Cheeseman, J. R.; Zakrzewski, V. G.; Montgomery, J. A., Jr.; Stratmann, R. E.; Burant, J. C.; Dapprich, S.; Millam, J. M.; Daniels, A. D.; Kudin, K. N.; Strain, M. C.; Farkas, O.; Tomasi, J.; Barone, V.; Cossi, M.; Cammi, R.; Mennucci, B.; Pomelli, C.; Adamo, C.; Clifford, S.; Ochterski, J.; Petersson, G. A.; Ayala, P. Y.; Cui, Q.; Morokuma, K.; Malick, D. K.; Rabuck, A. D.; Raghavachari, K.; Foresman, J. B.; Cioslowski, J.; Ortiz, J. V.; Stefanov, B. B.; Liu, G.; Liashenko, A.; Piskorz, P.; Komaromi, I.; Gomperts, R.; Martin, R. L.; Fox, D. J.; Keith, T.; Al-Laham, M. A.; Peng, C. Y.; Nanayakkara, A.; Gonzalez, C.; Challacombe, M.; Gill, P. M. W.; Johnson, B. G.; Chen, W.; Wong, M. W.; Andres, J. L.; Head-Gordon, M.; Replogle, E. S.; Pople, J. A. *Gaussian 98*, revision A.9; Gaussian, Inc.: Pittsburgh, PA, 1998.

(95) Becke, A. D. *Phys. Rev. A* **1988**, *38*, 3098.

(96) Becke, A. D. *J. Chem. Phys.* **1993**, *98*, 5648.

(97) Lee, C.; Yang, W.; Parr, R. G. *Phys. Rev. B* **1988**, *37*, 785.

(98) Miehlich, B.; Savin, A.; Stoll, H.; Preuss, H. *Chem. Phys. Lett.* **1989**, *157*, 200.

Hay−Wadt basis set for Re, augmented by two f-polarization functions with exponents 0.5895 and 0.2683, as described by Rösch et al.[99] The default "extrafine" grid was used in all DFT computations. Harmonic vibrational frequencies[100] were calculated analytically, on geometries optimized with imposed O_h symmetry, and were unscaled.

All computed vibrational frequencies are real (i.e., energy minimum). RMS deviations between calculated and experimental frequencies (listed in Tables 4−6) increase in the order HF ≈ Becke3LYP < BLYP; the same trend governs the optimized geometries. Raman peak intensity calculations using the enhanced basis set were not attempted for DFT calculations, and nonresonance Raman intensities were examined with the smaller Hay−Wadt basis set to mitigate computational expense. Experimental and calculated relative intensities in Tables 4−6 are the ratio of the area of each peak to the area of the intense peak for the totally symmetric S_8 breathing mode at ~430 nm. Raman peaks at 263, 227, and 291 cm^{-1} for **1**; ~275 cm^{-1} for **2**; and 269 and 283 cm^{-1} for **3** overlap significantly. For these peaks, the sums of predicted Raman activities are compared to the combined areas of the overlapping experimental bands. Intensities of the calculated A_{1g} rhenium-halide breathing vibrations (222, 151, and 105 cm^{-1} in **1**, **2**, and **3**, respectively) are underestimated (11−25% of observed value) relative to that of the S_8 breathing mode. An intensity-stealing mechanism is insupportable because the experimental A_{1g} halide breathing modes span some 114

cm^{-1}, while the intense S_8 mode is nearly invariant. Discrepancies between calculated and experimental Raman intensities are entirely due to approximations in the calculation. Extended Hückel calculations were executed within the program Cacao,[101,102] using default parameters.[103]

Supporting Information Available: Tables of Mulliken populations for **1**−**3** and **13** and of observed and calculated vibrational frequencies of **1** and **13** using an enhanced basis set, deconvolution of the emission profile of **1**, and Raman spectra of **6**−**9**. This material is available free of charge via the Internet at http://pubs.acs.org.

JA0286371

(99) Gisdakism P.; Antonczak, S.; Rösch, N. *Organometallics* **1999**, *18*, 5044.
(100) Fogarasi, G.; Pulay, P. *Annu. Rev. Phys. Chem.* **1984**, *35*, 191.

(101) Mealli, C.; Proserio, D. M. *J. Chem. Educ.* **1990**, *67*, 399.
(102) Mealli, C.; López, J. A.; Sun, Y.; Calhorda, M. J. *Inorg. Chim. Acta* **1993**, *213*, 199.
(103) Alvarez, S. *Tables of Parameters for Extended Hückel Calculations*; Departmento de Quìmica Inorgànica, Universitat de Barcelona, 1989.